

Frictional melting of peridotite and seismic slip

P. Del Gaudio¹, G. Di Toro^{1,2}, R. Han³, T. Hirose⁴, S. Nielsen¹, T. Shimamoto⁵, A. Cavallo¹

¹ Istituto Nazionale di Geofisica e Vulcanologia, Sezione di Sismologia e Tettonofisica, Roma 00143, Italy

² Dipartimento di Geoscienze, Università degli Studi di Padova, Padova 35137, Italy

³ Department of Earth and Environmental Sciences, Korea University, Seoul 136-701, South Korea

⁴ Kochi Institute for Core Sample Research, JAMSTEC, 200 Monobe-otsu Nankoku, Kochi, 783-8502, Japan

⁵ Department of Earth and Planetary Systems Science, Hiroshima University, Higashi-Hiroshima 739-8526, Japan

Abstract

The evolution of the frictional strength along a fault at seismic slip rates (about 1 m/s) is a key factor controlling earthquake mechanics. At mantle depths, friction-induced melting and melt lubrication may influence earthquake slip and seismological data. We report on laboratory experiments designed to investigate dynamic fault strength and frictional melting processes in mantle rocks. We performed 20 experiments with Balmuccia peridotite in a high-velocity rotary shear apparatus and cylindrical samples (21.8 mm in diameter) over a wide range of normal stresses (5.4 to 16.1 MPa), slip rates (0.23 to 1.14 m/s) and displacements (1.5 to 71 m).

During the experiments, shear stress evolved with cumulative displacement in five main stages (stages 1-5). In stage 1 (*first strengthening*), the coefficient of friction μ increased up to 0.4-0.7 (first peak in friction). In stage 2 (*abrupt first weakening*) μ decreased to about 0.25-0.40. In stage 3 (*gradual second strengthening*) shear stress increased towards a second peak in friction ($\mu = 0.30-0.40$). In stage 4 (*gradual second weakening*) the shear stress decreased towards a *steady-state* value (stage 5) with $\mu = 0.15$. Stage 1 and stage 2 are of too short duration to be investigated in detail with the current experimental configuration. By interrupting the experiments during stages 3, 4 and 5, microstructural (FE-SEM) and geochemical (EPMA and EDS) analysis of the slipping zone suggest that *second strengthening* (stage 3) is associated with the production of a grain-supported melt-poor layer, while *second weakening* (stage 4) and *steady-state* (stage 5) with the formation of a continuous melt-rich layer with an estimated temperature up to 1780 °C. Microstructures formed during the experiments were very similar to those found in natural ultramafic pseudotachylytes.

By performing experiments at different normal stresses and slip rates (1) the “thermal” (as it includes the thermally activated first and second weakening) slip distance to achieve steady-state from

the first peak in strength decreased with increasing normal stress and slip rate, (2) the steady-state shear stress slightly increased with increasing normal stress and, for a given normal stress, decreased with increasing slip rate. The ratio of shear stress vs. normal stress was about 0.15, well below the typical friction coefficient of rocks (0.6-0.8). The dependence of steady-state shear stress with normal stress was described by means of a constitutive equation for melt lubrication.

The presence of microstructures similar to those found in natural pseudotachylytes and the determination of a constitutive equation that describes the experimental data, allows extrapolation of the experimental observations to natural conditions and to the study of rupture dynamics in mantle rocks.

Keywords: Pseudotachylyte; Peridotite; Frictional melting; Thermal slip distance; Earthquake; Fault rheology

1. Introduction

Earthquake dynamics is concerned with both the behavior of the volume around the fault including accumulation of elastic strain energy and catastrophic release thereof [Reid, 1910], and the behavior of the fault itself as a contact problem in which understanding fault friction [Scholz, 2002] and shear fracture [Ohnaka, 2003] is a key. In particular, if the frictional resistance in the slipping zone decreases with increasing displacement, earthquakes may occur [Scholz, 2002; Rice, 2006]. It follows that it is of great relevance to determine how frictional strength evolves with slip and slip rate under the extreme deformation conditions typical of earthquakes (stresses normal to the fault as large as hundreds of MPa, slip rates up to 10 m/s and displacements up to 20 m) [e.g., Heaton, 1990]. Though it is not possible to reproduce such deformation conditions with the current experimental apparatuses [Di Toro et al., 2006b; Tullis, 2008], experimental work has been carried out during the last twenty years to simulate at least some combination of these variables, like normal stress and displacement [Beeler et al., 1996; Goldsby and Tullis, 2002] or slip rate and displacement [Spray, 1987; 1995; 2005; Tsutsumi and Shimamoto, 1997; Hirose and Shimamoto, 2003; 2005; Hirose and Bystricky, 2007; Di Toro et al., 2004; 2006a; 2006b; Han et al., 2007a; 2007b; Mizoguchi et al., 2007; Boutareaud et al., 2008]. Within the many cohesive (gabbro, tonalite, marble, quartzite, monzodiorite, serpentinite, etc.) and non-cohesive (clay-rich gouges) rocks investigated in high-velocity friction experiments, peridotite, the typical upper mantle rock, has not been studied yet, though earthquakes occur at mantle depths in extensional, contractional and strike-slip settings [e.g., Frohlich, 2006]. In particular, field evidence suggests that friction-induced rock melting may be typical in mantle rocks [Obata and Karato, 1995; Andersen and Austrheim, 2006; Andersen et al., 2008; Piccardo et al., 2008] at mantle depths [Ueda et al., 2008]. This is confirmed by torsion experiments under high normal stress (5 GPa) performed in the 1930s [Bridgman, 1936] and theoretical studies [Griggs and Handin, 1960; Ogawa, 1987; Keleman and Hirth, 2007; Braeck and Podladchikov, 2008; John et al., 2009]. Though the mechanics of deep earthquakes remains enigmatic [Frohlich, 2006], production of frictional melts and melt lubrication is invoked based on seismological observations and energetic considerations in the case of the large deep-focus Bolivian M_w 8.2 1994 earthquake [Kanamori et al. 1998; Bouchon and Ihmlé, 1999]. Lastly, the investigation of frictional behavior (of peridotite in this case) at seismic slip rates, may also facilitate derivation of a (high-velocity) rock friction constitutive law to apply in rupture dynamics models [Fialko and Khazan, 2005; Nielsen et al., 2008].

Here we investigate the frictional properties of peridotite at realistic seismic slip rates and net displacements but lower normal stresses than expected at relevant depths. We describe microstructures produced during the experiments and investigate the evolution of fabric within the slipping zone as a function of increasing displacements. Lastly, we fit the experimental data with theoretical curves for melt lubrication and, since the microstructures produced in the experiments are similar to those found in natural pseudotachylytes, we extrapolate the experimental results to natural conditions.

2. Experimental methods

We used cored samples from a single block of the Balmuccia peridotite from the Ivrea - Verbano zone (Northern Italy) for all experiments described in this study. The peridotite block, free from any visible fractures and veins was collected from a quarry located at ~200 m northeast from the ultramafic pseudotachylytes-bearing outcrop along the Sesia river described in Obata and Karato [1995] and Ueda et al. [2008]. The peridotite has an average grain size of 0.7 mm and its modal composition is reported in Table 1.

We determined the mechanical properties of peridotite-bearing faults at seismic slip rates using a rotary shear high-velocity rock-friction (HVRF) apparatus [see details in Hirose and Shimamoto, 2005]. We prepared a pair of mushroom-shaped cylindrical specimens with diameter of 21.8 (sliding surface) and 24.8 mm (specimen holder side) and a length of about 23 mm each (Fig. 1a). We ground the specimen surfaces using a 400-grit diamond wheel. An aluminum ring (with an internal diameter of 21.85 mm, an external diameter of 25 and ~10 mm in length) was mounted to the thinner diameter of each specimen to prevent thermal fracturing of the samples due to grain expansion during rapid frictional heating. The length of each aluminum ring was ~1 mm shorter than the length of the specimen to avoid aluminum-aluminum contact during sliding which would alter the mechanical data. The cylindrical shape of specimens and the sustaining effect of the aluminum rings allowed the application of normal stresses up to ten times larger than those achieved in previous HVRF experiments [e.g., Tsutsumi and Shimamoto, 1997; Hirose and Shimamoto, 2005]. The application of large normal stresses up to 16 MPa, was necessary to induce frictional melting of peridotite, given the high melting temperature at 1-atm and dry conditions of the peridotite minerals: 1720 °C for olivine (Fo85) from the Balmuccia peridotite, 1550 °C for enstatite, 1392 °C for diopside and 1850 °C for spinel [Philpotts, 1990; Spray, 1992].

The specimens were placed in the sample holder and then mounted into the apparatus (Fig. 1b). After the installation, the peridotite surfaces were slid at a slip-rate of ~40 mm/s under a normal stress of ~0.8 MPa to produce full contact between the two surfaces. Wear materials produced on the surfaces during the pre-sliding were removed with a vacuum cleaner and a brush.

Each experiment consisted of four main steps (1 – 4): (1) application of normal stress; (2) we brought the rotary motor to the target speed while an electromagnetic clutch separated the rotating column from the specimen. When the motor speed reached the target value, (3) we switched on the electromagnetic clutch and the specimens started to slide; (4) we switched off the motor to end the experiment (a movie of a typical experiment is shown as supplement material). The number of rotations, the axial force, the axial shortening of the specimen and the torque were recorded by a digital recorder with a data sampling rate of 200 Hz.

Since slip rate increases with sample radius r in cylindrical samples ($v = \omega \cdot r = 2 \cdot \pi \cdot \gamma \cdot r$, where ω is the rotary speed and γ is the revolution rate of the motor), we introduced the “*equivalent slip rate*” v_e [Shimamoto and Tsutsumi, 1994]:

$$v_e = \frac{4 \cdot \pi \cdot \gamma \cdot r}{3} \quad \text{eq. 1}$$

We refer the equivalent slip rate simply as slip rate hereafter.

We performed 20 experiments divided in series A (Table 2) and B (Table 3). All the experiments were conducted under room temperature, room humidity, and unconfined conditions. In experiments HVR652, HVR676 and HVR677, we measured the temperature in the slipping zone with a radiation thermometer located at about 20 cm from the sliding surface. To check the role of oxidation of olivine during frictional heating and melting, we sealed the sample chamber, inserted a O₂ sensor and performed an experiment (HVR651) under argon flux (flow rate: 5 L/min). Series A experiments were performed at normal stresses between 5.4 and 16.1 MPa (i.e., the normal stress was kept constant during each experiment), slip rates between 0.23 and 1.14 m/s (i.e., the slip rate was changed during some experiments), and slip distances between 24 and 71 m. Series A experiments were conducted to investigate the dependence of (1) shear stress and, (2) shortening rate on normal stress and slip rate during frictional melting (Fig. 2a, Table 2). Series B experiments were performed under a fixed normal stress (13 MPa) and slip rate (1.14 m/s), but they were ended at slip distances ranging from 1.53 m (HVR675) to 31.31 m (Fig. 2b, Table 3). Series B experiments were conducted to investigate the microstructural and mineralogical evolution of the slipping zone materials with shear stress and slip. After the experiment, we prepared thin sections cut orthogonal to the slipping zone and located at ~3 mm from the outer surface of the specimen (Fig. 1a) to carry out microstructural, mineralogical and geochemical analyses (section 3.2).

3. Results

3.1. Mechanical data

3.1.1. Shear stress evolution with slip

The typical shear stress versus slip curve for simulated faults in peridotite at slip rates of ~1 m/s is shown in Fig. 2a (HVR644 performed at a normal stress of 13 MPa). During the experiments, shear stress evolved with displacement in five stages (1-5). Initial *first strengthening* (0 – a, stage 1) was followed by an abrupt *first weakening* (a to b, stage 2). Then, shear stress increased during a

second strengthening (b to c, stage 3) stage followed by a gradual *second weakening* (c to d, stage 4) towards a *steady-state* value (d to e, stage 5). This shear stress evolution with increasing slip for peridotite is similar to that reported in experiments conducted on gabbro under lower normal stress (~1.3 MPa) but for similar slip rates (~0.85 m/s) [Tsutsumi and Shimamoto, 1997; Hirose and Shimamoto, 2005]. In HVR644, when the slip rate decreased from 0.92 to 0.61 m/s, the steady-state shear stress concurrently increased from 1.7 to 2.2 MPa (point e-f). A similar slip rate dependence was observed at the end of the experiment (point g), when the shear stress increased as the slip decelerated once the rotary column was disconnected from the motor.

During the experiment, gouge forms due to wear of the fault surfaces. The shortening rate v_{short} , which includes abrasive wear and melting of the specimens, is in all the experiments < 0.1 mm/s. Debris is extruded from the fault at the beginning of slip, until about point b in Fig.2a. After point b, gouge extrusion ceases and the slipping zone flashes intermittently during the slip-hardening stage b to c. Visible frictional melting with abundant extrusion of drops of melts starts from about the second peak strength (point c). During the transient towards steady-state (c to d) and during steady-state shear stress (d to e and f to g), melt drops are continuously extruded from the slipping zone. Once the magnetic clutch was turned off at point g to end the experiment, the specimen rotated for other 1.2 m due to the inertia of the rotary column (Fig. 2a). During this final slip, when slip rate decreased from 0.61 to 0 m/s, the fault strengthened by 0.8 MPa. By increasing the total slip, the magnitude of strength recovery at the end of each experiment decreased from 8 MPa for 2.77 m of slip (HVR672) to 2.9 MPa for 30.50 m of slip (HVR620) (Fig. 2b). Temperatures of the outer surface of the slipping zone were measured by means of a radiation thermometer. In the case of HVR652, performed at a slip rate of 1.14 m/s and a normal stress of 13 MPa, temperature increased during the first and second weakening towards an almost constant value of 1100~1300 °C (corresponding to the steady-state shear stress) (Fig. 2c).

To determine the effect of oxidation on the dynamic fault strength, we compared experiments conducted at the open air (O₂ concentration 21 %) and under argon flux (O₂ concentration 0.4 %) (Fig. 2c). At steady-state, the difference between the experiment conducted under argon flux (HVR651) and that in open air (HVR620) was less than 0.5 MPa, which corresponded to a difference of < 0.04 in the friction coefficient. This small difference was of the same order of magnitude found for repeated experiments conducted at the open air under identical slip rates and normal stresses (e.g., HVR620 and HVR641, the latter not shown in Fig. 2c).

3.1.2. The thermal slip distance

The critical slip distance d_c (or slip weakening distance in the case of velocity weakening materials) has a formal definition in the rate and state friction law [e.g., Marone, 1998; Scholz, 2002]. In experiments performed in biaxial and triaxial apparatuses for displacements of few centimeters and

slip rates of few millimeters per second (i.e., where experimental results are described by the rate and state friction law), d_c is of 10-500 μm [Paterson and Wang, 2005 for a review]. In these low slip rate experiments, d_c scales roughly with surface roughness (i.e., size of the asperities) or, in the presence of gouges, particle size and gouge thickness [Dieterich and Kilgore 1994; Marone and Kilgore, 1993]. However, in the case of experiments performed under seismic deformation conditions (and in real earthquakes [Ide and Takeo, 1997]), weakening occurs over distances of the order of meters and is related to the thermal evolution of the slipping zone rather than to the roughness of the sliding surface [Hirose and Shimamoto, 2003; Rice, 2006; Di Toro et al., 2006b]. For instance, in the peridotite experiments described in this study, τ_{ss} is achieved after two slip weakening stages (the first of short duration, a to b, and the second long-lasting, c to d, Fig. 2a) interpreted as the result of two different thermally activated processes (flash heating and melt lubrication, respectively, see section 4.2). To describe this long duration weakening, which is related to (1) temperature increase and, (2) dramatic physical changes in the slipping zone, we introduce the thermal slip distance d_{th} defined as the slip distance on the best-fit smoothed curve of the shear stress evolution with slip over which the shear stress τ_{th} reduces to:

$$\tau_{th} = \tau_{ss} + 0.05 \cdot (\tau_i - \tau_{ss}) \quad \text{Eq. 2.}$$

The best -fit smoothed curve of shear stress vs. slip was obtained by means of a central moving average of the shear stress values over a window of 100 acquired data. In the case of the experiment show in Fig. 2a, the sampling rate was 200 Hz and the 100 acquired data correspond to 0.5 m in slip from point a to e and 0.3 m from point f to g. In some experiments (e.g., HVR635 in Table 2), large errors in the determination of d_{th} are due to the scatter of the shear stress experimental data with respect to the smoothed curve (error is defined as the minimum and maximum slip distance on the scattered data of the shear stress evolution curve with slip, equivalent to τ_{th} on the best-fit smoothed curve). The d_{th} was determined for experiments performed at different slip rates but constant normal stress (Fig. 3a) and for experiments at a constant slip rate but different normal stresses (Fig. 3b). Although data are scattered, they indicate that d_{th} decreased from 22 m to about 5 m with increasing slip rate (Fig. 3a) and from 37 m to about 5 m with increasing normal stress (Fig. 3b). Theoretical arguments suggest that the duration of d_{th} should scale with $1/(\tau \cdot v_e)^2$ and – in case of approximate proportionality between traction and normal stress (σ) in the slip initial phase – it should scale with $1/(\sigma^2 \cdot v_e)^2$, resulting in $d_{th} \propto 1/(\sigma^2 \cdot v_e)$ (see Fig. 3c and discussion in section 4.2.3).

3.1.3. Normal stress and slip rate dependence of fault strength

In Fig. 4a we report shear stress at the initial peak (τ_i), second peak (τ_{2nd}) and steady-state (τ_{ss}) versus normal stress for experiments performed at a constant slip rate of 1.14 m/s. Shear stress at the three different stages increased with normal stress (σ_n). Shear stress at the initial and second peaks approximately follows the empirical linear relationship $\tau_i = 0.6 \cdot \sigma_n$ and $\tau_{2nd} = 2.13 + 0.21 \cdot \sigma_n$ respectively. Shear stress at the steady-state can be fit by the theoretical equation for frictional melting [Nielsen et al., 2008]:

$$\tau_{ss} = m \cdot (\sigma_n - \sigma_0)^{0.25} \quad \text{eq. 3}$$

where m and σ_0 are constants. The best fitting for the steady-state shear stress with the equation yields $m = 1.14 \pm 0.07$ and $\sigma_0 = 4.69 \pm 0.68$ MPa (Fig. 4a). According to our experimental data, fault strength at the second peak and at steady-state is well below the Byerlee's friction ($\tau = 0.85 \div 0.6 \cdot \sigma_n$, shaded area in Fig. 4a).

The dependence of the shear stress at the second peak and during steady-state with slip rate is shown in Fig. 4b. The shear stress at second peak is almost independent to slip rate: the slope (τ / v_e) of the best fit line for shear stress versus slip rate is -0.03 (MPa/m/s). Instead, steady-state shear stress decreased with increasing slip rate. In the presence of frictional melts, the velocity dependence of the steady-state shear stress is described by [Nielsen et al., 2008]:

$$\tau_{ss} = \sigma_n^{0.25} \cdot \frac{A}{\sqrt{r}} \cdot \sqrt{\frac{\log(2v_e / W)}{v_e / W}} \quad \text{eq. 4}$$

where W is a characteristic velocity and A is a scaling group of several parameters including the effect of normal stress. For such a weakening law, a satisfactory fit was obtained by using $W = 0.076$ m/s and $A = 8.35$ MPa (Fig. 4b).

3.2. Microstructure and geochemistry

To investigate the physico-chemical processes responsible for the strengthening and weakening of the peridotite-bearing faults at seismic slip rates, we performed the Series B experiments at constant slip rate and normal stress, and stopped the experiments at different slip distances. We limit our description to the most relevant microstructural and geochemical features and how they evolve with increasing slip. Microstructures of simulated fault zones and wall rocks were investigated under a Field Emission Scanning Electron Microscope (FE-SEM) JSM6500F upgraded to version 7000. The chemical compositions of grains and glasses were determined on carbon-coated, polished thin sections

using an Electron Probe Micro-Analyzer (EPMA) JEOL JXA8200 (INGV, Rome) and a CAMECA SX50 (Istituto di Geoscienze e Georisorse, Padua) with a focused beam about 1 μm in diameter under accelerating voltage of 15 kV and current 15 nA. Images analysis of simulated fault zones show grains (fragments and microlites) occupying over 70 % of the slipping zone (Fig. 5 and Table 3). This large distribution of grains reduced the area occupied by glass –in small pockets. Since EPMA beam spot size for analysis is larger than glass pockets we conducted a semi-quantitative analysis with the FE-SEM equipped with an Energy dispersive X-ray spectroscopy (EDS) analyzer. The EDS electron beam spot size for analysis was about 400 nm as estimated by means of Monte Carlo Method simulations and from analysis performed on triple grain junctions between olivine, diopside and enstatite. Though EDS analyses are semi-quantitative, the performed EDS analyses approximate EPMA analyses, as shown by the composition of olivine grains from the wall rocks determined with the two analytical techniques (Table 4).

3.2.1 *The slipping zone*

The slipping zone consists of grains of olivine, pyroxenes (diopside and enstatite) and Cr-spinel (Tables 1 and 4) immersed in a glass+gouge- (only in the case of HVR675) and glass-supported (all the other experiments) matrix. The shape, type and composition of the grains varied with increasing slip. Section 3.2.2 and Table 5 describe the glass chemistry.

In the shortest experiment, HVR675 (slip = 1.53 m), stopped during the second strengthening (section b-c in Fig. 2a), the gouge is made of fragments of olivine, diopside, enstatite and spinel immersed in a gouge-supported (submicron in size) matrix. The gouge is partially welded by ultra-thin layers and micro-patches of glass (usually 100 nm in thickness) with pumiceous and bubbly aspect (Fig. 5a). Small and large grains of olivine are rounded. FE-SEM EDS transects of olivine grains indicate a systematic zoning, with a Fe-rich core and a Fe-poor rim (Fig. 6a). The FeO content at the core of the olivine grains is consistent with that found in olivine in the host rock (compare with table 4). In Fig. 6 we also reported the CaO content (in wt %) in olivine though CaO has a large standard deviation (Table 4). However, such large standard deviation is the result of EDS analysis randomly conducted in different positions of the olivine grains. Instead, a systematic analysis along transects of olivine grains (Fig. 6) shows that CaO content is constant in all investigated grains. The slight increase of CaO content at the rim of the olivine grain is due to analyses contamination (the beam spot size is 400 nm) by the nearby glass (i.e., the glass is enriched in CaO, see section 3.2.2). Instead, in the case of analyses acquired inside the grain (i.e., at more than 400 nm from the grain border), the CaO concentration is independent of FeO content (Fig. 6). It follows that FeO analyses from the inner part of the olivine grain were not contaminated by a non spherical, 3D geometry of the grain (e.g., by the presence of deep embayments filled by melt inside the grain). In experiment HVR672 (slip = 2.77 m), stopped at approximately the second peak in shear stress, enstatite, spinel and olivine grains are

immersed in a glass-supported matrix (Fig. 5b-d). The gouge-supported matrix is locally preserved in few pockets (not shown), and included few clasts of diopside, which are absent in the glass-supported matrix. Small olivine grains have usually straight grain boundaries, euhedral shape and are zoned (Fig. 5d), with a Fe-rich core and a Fe-poor rim (same zoning as in HVR675). Large olivine grains are often rounded and olivine grain size decreases from the inner part of the slipping zone towards the wall rocks (Fig. 5c). Typically, the olivine and enstatite in the wall rocks have the interface with the melt darker in color, due to diffusion loss of Fe and initial melting: in the case for the large olivine grain shown in Fig. 5c, the FeO content decreased from 9.73 % at the core to 7.30 % at the rim. Euhedral and non-euhedral olivine grains are also found in narrow injection veins (Fig. 5d).

Experiments HVR671 (slip with 5.70 m), HVR673 (slip with 9.90 m), stopped during the second weakening, and experiments with large displacements as HVR620 (slip with 30.50 m), stopped during the steady-state, have microstructures similar to those found in HVR672 (Fig. 5e-f). Grains of olivine, spinel and enstatite are immersed in a glass-supported matrix. The main difference with HVR672 is the absence of the gouge-supported matrix. Large and small olivine grains have straight edges, and in most cases, they are euhedral. Micron in size euhedral enstatites are locally developed.

In the case of large displacements experiments, as HVR620, zoned olivine grains (Fig. 6b) are very similar to those found in short duration experiments (HVR675, Fig. 6a), also for the total FeO content, though the grains have straight edges. Small (<5 μm in size) olivine grains are usually euhedral (see also Fig. 5g from HVR644 slip 43.60 m) and have FeO content lower (< 7 % on average, Fig. 6c) than FeO in olivine from the wall rocks (about 9 %, Table 4). In the case of large displacements (> 30.50 m) experiments, we also found widespread crystallization of diopside, often nucleating on olivine and enstatite walls (Fig. 5g).

As evident from the FE-SEM images (Fig. 5), grains (microlites and fragments) occupy > 70 % of the slipping zone in all the samples, independently of the total slip (Table 3). Bubbles with ~1 to 10 μm in size were found in the slipping zone of all the experiments. The amount of bubbles is higher (up to ~5 %) at the border of the specimen and their abundance is nearly constant for all runs, independently of the cumulated slip. As no hydrous minerals were present in the peridotite (Table 1), the bubbles are due to air or gas (bubbles were also observed in HVR651 conducted under argon flux) trapped at the beginning or, in the case of the external part of the specimen at the contact with the open air, during the experiment.

At the end of each experiment, the two specimens of peridotite are separated by a 60 to 130 μm thick slipping zone (Fig. 7). We determined the thickness of the slipping zone on an optical microscope by measuring every 0.5 mm the distance between the opposite wall rocks and by averaging these values. The average thickness of the slipping zone increased with increasing slip (series B experiments, Table 3) from 65.9 μm (glass + gouge supported matrix, HVR675, 1.53 m of slip) to 131.1 μm (glass-supported matrix, HVR620, 30.50 m of slip).

Fractures filled by glass and by microlites (mainly olivine) are observed in the wall rocks sandwiching the slipping zone (Fig. 5c, h). Glass veins cut a single mineral (olivine, pyroxene or spinel) or are at the contact of two or three minerals. Veins are parallel to orthogonal with respect to the slipping zone (in a two-dimensional view), propagating from 10-20 μm in the case of short duration experiments (HVR675, 1.53 m of slip, not shown) up to 900 μm for large slip experiments (HVR620, 30.50 m of slip, Fig. 5h).

3.2.2 Glass chemistry

Given the abundance of microlites and fragments inside the glass that may contaminate the EPMA analyses and the accuracy of the EDS analyses (which has a smaller spot size than the EPMA beam), we produced about one thousand EDS analyses of the glass from (1) the slipping zone and (2) veins hosted in the wall rocks (inside olivine grains, at the contact between olivine-diopside, olivine-spinel, enstatite-olivine, etc.). The averages of selected representative analyses (about one hundred) of the EDS data are shown in Table 5.

In the slipping zone, glass composition changed with (1) the position inside the sample (as suggested by the variations in color in BSE (back scattered electrons) images, e.g., Fig. 5f) and, for some elements like SiO_2 and CaO , (2) total slip (Table 5, group 1, Fig. 8a-b).

In experiment HVR675 (1.53 m of slip), the composition of the glass matrix is highly variable in the slipping zone, and includes MgO-poor thin patches (Table 5, group 1) and MgO-rich, ultrabasic patches rimming olivine grains (Table 5, group 2). The latter glass is typical of the slipping zone of this (short duration) experiment. In the other experiments this was found only in the wall rocks (HVR620 and HVR673, Table 5, group 2). In experiment HVR672 (2.77 m of slip) the most common glass is enriched in SiO_2 and MgO (usually darker in color than the neighboring olivine grains) with respect to the HVR675 “dominant” glass (Table 5, group 1). In experiment HVR673 (slip = 9.90 m), the dominant composition of the glass is further enriched in SiO_2 and CaO and approximates the composition of large slip experiments (e.g., HVR620, Table 5, group 1).

The wall rocks host glass veins (Fig. 5c, h). In most cases, independently of the duration of the experiment and the composition of the neighbor grains, the veins are bright in color (Fig. 5c, h), reflecting enrichment in CaO with respect to enstatite and olivine (compare in Table 5, groups 3, 4, 5, 6, 7 with EPMA data from Table 4). The composition of the glass approximates that for diopside when at the contact with diopside grains (Table 5, group 9). Micron in size euhedral grains of enstatite and olivine are found in most glass veins, up to a distance of 1 mm from the slipping zone.

4. Discussion

The experimental data (i.e., the low magnitude of the shear stress and the slight dependence of shear stress with normal stress) and the occurrence of glass in the slipping zone, indicates that the weakening mechanism in the peridotite experiments is melt lubrication [Hirose and Shimamoto, 2005; Di Toro et al., 2006a]. Here below we first discuss the main parameters that control melt lubrication (e.g., clast content, melt temperature and composition, melt viscosity, thickness of the slipping zone, Persson, 2000; Nielsen et al., 2008), then the fault processes involved in the evolution of fault strength with cumulated slip and, finally, the extrapolation of experimental results to natural conditions.

4.1. Inherited and newly grown olivine grains, estimate of the melt temperature, glass composition and melt viscosity

The fraction of solid particles in the molten zone ranges between 54-78 % (Table 3). In the case of olivine, the FE-SEM and EDS analyses indicate the presence of at least two types of grains: (1) zoned grains (e.g., LG5 in Fig. 6a), interpreted as inherited grains and (2), non-zoned grains (e.g., LG13 and LG14 in Fig. 6c) interpreted as newly formed grains.

Zoned grains have a FeO-rich (FeO about 9-10 % in wt., which corresponds to olivine Fo82, and a FeO-poor rim (FeO about 8 % in wt., which corresponds to olivine Fo85). The composition of the core is the same as that of olivine in the host rock (Fo82-85). It follows that zoned grains are the result of fragmentation of the olivine grains from the former peridotite. Zoning is consistent with heating and diffusion loss of Fe from the external part of the olivine grain during initial sliding, frictional heating and grain interaction with the melt. In the case of experiments for slip larger than 2.7 m, zoned grains have often straight edges of bright color which might suggest olivine overgrowth of a very thin (< 100 nm, below the resolution of the FE-SEM EDS) FeO rich rim during cooling (Fig. 5b, 5d, 5f).

Non-zoned olivine grains are often euhedral (Fig. 5g) and have a FeO-poor core (FeO about 4-6 % in wt., which corresponds to olivine Fo90-92). Their Fo92 content, higher than in olivine from the host peridotite, suggests that these olivine crystallites (e.g., Fig. 5g) were grown from the frictional melt at temperatures as high as 1780 °C.

The composition of the newly formed olivine crystallites yields a more realistic estimate of the friction melt temperature (1780 °C) with respect to the temperature measured with the radiation thermometer (~1300 °C towards the steady-state, see Fig. 2c). The measured temperature is lower than (1) the melting point of rock-forming minerals of peridotite at 1-atm (> 1400 °C, see section 2) and (2) the possible peritectic melting temperature for the system olivine-enstatite (1530 °C, Philpotts, 1990). The radiation thermometer measures the temperature over a spot size of 400 µm in diameter whereas the slipping zone (= glass) thickness measured at the end of the experiment was ~180 µm thick (e.g., Fig. 7). It follows that the measured temperature averages the wall rocks and the slipping zone temperatures, and the measured temperature yields a lower limit to the melt temperature. The melt

temperatures estimated from newly grown olivine (1780 °C) are higher than the melting temperature of all the peridotite-forming minerals (with the exception of spinel), including olivine from the host peridotite (Fo82-Fo85, melting temperature 1680-1720 °C). The achievement of such extremely high temperatures may be explained by “super-heating” of the frictional melt due to shearing of a viscous fluid [Di Toro and Pennacchioni, 2004; Nielsen et al., 2008].

The glass composition in the slipping zone evolves with displacement towards the SiO₂- and CaO-rich compositions found in the glass veins hosted in the wall rocks (Fig. 8, Table 5 Group 1). During the experiment, the thermal pulse diffuses through the inner part of the specimen (the more distant glass veins are found in the long lasting experiments, Fig. 5h) and diopside, the mineral with the lowest melting point, is the first mineral to melt. Once produced (glass veins in the wall rocks are produced *in situ*), the CaO-rich melt migrates along grain boundaries and fractures and eventually mixes and mingles with the melt produced in the slipping zone at higher temperatures. The presence of melt along grains also weakens the host peridotite allowing large un-sustained grains to collapse into the slipping zone (Fig. 5h). It is also possible that peritectic melting (1530-1500 °C, [Philpotts, 1990]) occurs at the olivine-enstatite contact in the wall rocks, as suggested by the high SiO₂ (60-62%) content found in some glasses (Table 5, groups 6-7).

Melt viscosity is the result of melt temperature, melt composition and clast content. The fraction of solid particles in the glass is up to 78 % in volume. For particle content > 60 vol. %, the rheology of a melt suspension behaves like a solid and is markedly non-Newtonian [Costa, 2005]. This rheology is not consistent with the mechanical data (Fig. 2), which, instead, suggests a low viscosity melt. Actually, the euhedral aspect of the grains and their zoning suggest microlite crystallization or overgrowth on survivor grains, probably at the end of the experiment (point g in Fig. 2a). It follows that the clast content during the experiment is unknown and the estimate the viscosity of the melt not possible.

4.2. Shear stress evolution with slip

4.2.1. First strengthening and first weakening

The HVFR experiments on peridotite indicate two stages of potentially unstable slip weakening behavior of a fault (first and second weakening) each preceded by a strengthening stage (first and second strengthening). In general, this frictional behavior is consistent with the one observed on gabbro at similar slip rates but at lower normal stresses (~1.3 MPa) [Hirose and Shimamoto, 2005]. Unfortunately, these experiments are not suitable for the investigation of the initial strengthening and weakening of the specimen, given the poor elastic stiffness of the apparatus, the absence of a steep loading step for the shear stress, and the utilization of small cylindrical samples. Last but not least, the Balmuccia peridotite is extremely difficult to work given his hardness compared to other rocks used in

high-velocity experiments (e.g., Carrara Marble, Han et al., 2007). Difficulties in sample preparation might result in not perfect alignment of the specimens even after the preliminary slid at a slip-rate of ~ 40 mm/s: if the two opposite surfaces are not fully parallel, stress concentration determine the failure of the sample edges at the initiation of sliding. The above experimental limitations and the heterogeneous distribution of normal and shear stress on the sliding surface, before bulk melting occurs, do not allow the accurate determination of the coefficient of friction at the initiation of slip (at least compared to biaxial apparatus, [e.g., Marone, 1998]).

During step 1 of the experiment (see section 2) the specimens are under normal load only. Given the limitations highlighted above, we can speculate that when samples are abruptly forced to rotate at effective velocities of about 1 m/s (step 3), the applied shear stress (i.e., the torque) has to overcome the static friction of peridotite and the frictional strength related to the non-perfect alignment of the samples. This might explain the large scatter of the first peak in friction (0.4-0.7), which, on average (0.6) approximates the typical value for the friction coefficient of peridotite (0.6-0.8, [Byerlee, 1978]).

First strengthening is followed by first weakening which occurs in few tens of centimeters at most (usually less than 10 cm). During this weakening stage, the sample is sliding at equivalent velocities between 0 and 1 m/s where velocity-dependent weakening mechanisms, such as flash heating at the asperity contacts [Rice, 2006; Rempel, 2006; Beeler et al., 2008] or silica gel lubrication [Goldsby and Tullis, 2002; Di Toro et al., 2004] might be activated. As shown by the movie taken during the experiment (see supplemental material), there is a large amount of gouge produced at the very beginning of the experiment. Compared to experiments performed on gabbro, this is probably the result of the large normal stress applied, as abrasive wear of rocks tends to be enhanced by (1) increasing normal stress [Scholz, 2002] and (2) power density (the product of shear stress with slip velocity). It follows that the first weakening observed in the peridotite experiments is likely to be associated with the frictional behavior of a gouge layer sheared at high slip rates. However, the formation of a gouge layer cannot explain, by itself, the dramatic first weakening, as friction experiments performed on gouges at low slip rates (< 1 mm/s) do not show such low frictional strengths [e.g., Marone, 1998]. It follows that one or more dynamic weakening mechanisms must be activated. The Balmuccia lherzolite has < 46 % in SiO_2 in weight [Obata and Karato, 1995], and experiments performed under argon fluxes (i.e., H_2O poor environments, HVR651) showed similar weakening to the experiments performed in the presence of room air (presence of H_2O). We conclude that the activation of silica-gel lubrication [Goldsby and Tullis, 2002; Di Toro et al., 2004] due to the interaction of H_2O with SiO_2 to produce gels can be ruled out. Instead, first weakening is probably due to flash heating at asperity contacts of the gouge particles [Rice, 2006; Rempel, 2006; Beeler et al., 2008]. However, our understanding of high-velocity gouge weakening is still poor and, given its relevance in earthquake nucleation, should be investigated in the future with specific experimental equipment.

4.2.2. *Second strengthening*

Strengthening up to a second peak followed the first weakening in all the experiments (b-c in Fig. 2a). Several experiments were performed either (1) at a given slip rate but under increasing normal stress (HVR 635, HVR634, HVR640, HVR633) or (2) at a given normal stress but for increasing slip rates (HVR642, HVR643, HVR645, HVR644, HVR641). The duration of the second strengthening decreases with either normal stress or slip rate. The magnitude of the second strength peak does not appear to vary with slip rate, but appears to increase with normal stress (Table 2) and can be fit by a line ($2.8 + 0.21 \cdot \sigma_n$ MPa) which is well below the friction coefficient for solid peridotite (Fig. 4a). The product of slip rate by normal stress equates to the energy exchanged on the sliding surface for unit time and unit area (or the power density). The peak strength and the duration of second strengthening appear to depend on the power produced on the slipping zone, which suggests some form of thermally activated mechanism. On the other hand, the decrease of the steady-state friction coefficient with increasing normal stress (Table 2) suggests lubrication in the presence of fluids [Persson, 2000]. Given the technical limitations of the apparatus, we could not analyze this process in detail, since the second strengthening occurs too early and is too short-lived for the experiment to be stopped at this stage. However, experiment HVR675 arrested after 1.53 m of slip (the minimum slip we were able to impose for a run with an initial effective velocity of 1.14 m/s), yields some insights about the mechanism involved during the second strengthening. In HVR675, gouge and melt coexist in the slipping zone (Fig. 5a). A very thin layer of glass (< 100 nm in thickness) wraps grains of olivine, enstatite and diopside, suggesting that strengthening is due to mixed lubrication related to the local formation of melt in a grain-supported matrix. In the slipping zone, (1) the ultrabasic composition of the glass near the olivine grains (melting point of Fo85 olivine at 1-atm is 1720 °C) (Table 5, group 2), (2) the presence of olivine grains with the rim depleted in FeO (Fig. 6a) and of survivor grains of diopside (melting point at 1-atm is 1390 °C) depleted in CaO, are indicative of non-uniform temperature distribution in the slipping zone and local melting at the grain contacts. This strengthening mechanism is different to that described in gabbro where microstructural observations of the slipping zone suggest second strengthening as the result of the formation and growth of thin melt patches, as thin melt patches are highly viscous and oppose a large shear resistance to sliding [Hirose and Shimamoto, 2005]. However, the decrease of the duration of second strengthening (and of the second peak in the friction coefficient) with increasing normal stress (Table 2), suggests that the braking effect of the second strengthening may not be significant at normal stresses typical of earthquakes nucleation depth (> 100 MPa), especially for deep crustal or upper mantle earthquakes (20-50 km depth, > 1 GPa).

4.2.3 *Second weakening and steady-state shear stress*

Upon reaching the second peak, shear stress decays in a quasi-exponential fashion until it reaches a relatively low, steady-state value. After the second peak the simulated fault is coated by a continuous and thin film of melt (Fig. 5b-d); from this point on, it is reasonable to describe the shear stress on the fault (or friction in a general sense) as the result of viscous shearing across a thin layer of melt with clasts in suspension. Such an exercise is not trivial, because two a-priori unknown parameters control the relative strength of the melt layer at a given slip velocity: the thickness of the melt layer and its viscosity. The thickness depends on the amount of melt produced, which is controlled by a complex heat balance at the melt/solid boundary (a moving boundary problem known as the Stefan problem), minus the amount of melt extruded (i.e., the centrifugal fluid flow motion mainly forced by the normal stress). The viscosity, on the other hand, is very strongly dependent on melt temperature, variability of clast content (which cannot be determined in this study given the presence of inherited fragments mixed with newly grown phases that might have crystallized after the experiment during cooling at room temperature) and may have a non-Newtonian behavior [Costa, 2005]. It can also be shown that both temperature and shear are not homogeneously distributed across the melt thickness.

The estimate of the shear stress at steady-state is easier to approach. In Nielsen et al. [2008] the problem of obtaining the viscosity and temperature distribution inside the melt layer, and the equilibrium thickness of the melt layer was solved for the steady-state condition. Thus it was possible to relate the shear stress at the steady-state on the fault to (1) the sliding velocity and (2) to the applied normal stress [power law dependence of shear stress on normal stress, eq. 4].

The investigation of the shear stress evolution during the transient is more difficult to approach. It was also shown by Nielsen et al. [2008] that the transient stress decay after the second peak is essentially controlled by the evolution of the thermal diffusion in the solid. Indeed the temperature of the melt becomes stable (and steady-state shear stress achieved) once the heat has diffused into a boundary layer of thickness κ/v_m , where κ is the thermal diffusivity and v_m is the migration velocity of the melt/solid boundary (half the sample shortening rate). However, the theoretical analysis above should hold provided that the heat loss other than melting, extrusion and diffusion within the rock is negligible. In the case of the present experiments, given that peridotite has quite high melting temperatures, and the durations of the experiment are considerably longer than for other rocks, a situation of diffuse high temperature throughout the sample (an in part on the sample holder) is reached, which considerably promotes the amount of heat loss through free-air radiation. The effect of radiation during high-velocity experiments in the presence of melt is discussed elsewhere [Nielsen et al., 2008], and it is shown that it can alter significantly the overall frictional behavior, unless the studied rock melts quickly and the shortening rate is relatively high (close to 0.5 mm/s or more), conditions which are achieved only if high velocity (> 0.5 m/s), high normal stress (> 5 MPa) and relatively low melting temperatures (< 1200 °C) are combined. This is obviously not the case for the experiments studied here (shortening rates < 0.1 mm/s), so that the comparison with the theoretical

predictions (e.g., eq. 4) are only qualitative. Indeed, the expected (bilateral) shortening rate v_{short} if radiation loss was negligible, should be proportional to heat production rate “ $\tau \cdot v_e$ ” at steady-state according to $v_{short} = \tau_{ss} \cdot v_e [\rho \cdot (L + c_p \cdot \Delta T)]$ where ρ is mass density, L latent heat, c_p heat capacity and ΔT the difference between initial temperature of rock at rest and melt temperature [Nielsen et al., 2008]. Using parameter values of peridotite and the experimental values for τ_{ss} and v_e the resulting shortening rate should be of the order of 1 mm/s, but the experimentally measured value is about ten times smaller (i.e., 0.1 mm/s), indicating that a considerable amount of heat is dissipated by radiation. We note that nonetheless, the observed qualitative behavior corresponds to that of melting dynamics as predicted by theory (Eq. 4) or observed in other experiments with reduced radiation loss [see Nielsen et al., 2008].

Theoretical arguments based on the solution of the Stefan problem (heat-flow with a migrating boundary due to melting), show that the duration t_w of the transient weakening towards the steady-state upon formation of melting at the frictional interface, should scale as $t_w \propto 1/(\tau \cdot v_e)^2$. This means that the inverse of the square of the frictional work rate or power density [Nielsen et al., 2008], provided that shear stress τ and velocity v_e are constant, or, if not constant, are represented by a significant constant average. The same scaling actually applies to the duration t_m required to reach initial melting under a given shear stress and velocity, i.e., $t_m \propto 1/(\tau \cdot v_e)^2$. As a consequence, the whole transient duration from onset of slip to steady-state (including the initial slip phase under relatively high shear stress with first and second peaks, with no pervasive melt, and final weakening in the presence of pervasive melt, leading to the steady-state), are somehow controlled by the product “ $\tau \cdot v_e$ ” and should scale with its inverse square. In addition, it is observed that shear stress at both first and second peak, and the general shear stress level in the initial phase, is approximately proportional to the applied normal stress (see Fig. 4, though the friction coefficient seems to vary depending on the state of advancement of the experiment). As a consequence, the shear stress curve in the whole initial phase leading to the steady-state, may be approximated by a series of time intervals t_i with stepwise constant shear stress, each of which follows a Coulomb friction law for a given coefficient: “ $\tau_1 = \sigma_n \cdot \mu_1$, $\tau_2 = \sigma_n \cdot \mu_2$, ..., $\tau_i = \sigma_n \cdot \mu_i$ ”. If the duration of each time interval t_i is inversely proportional to $(\tau_i \cdot v_e)^2$, as discussed above, then it is also inversely proportional to $(\sigma_n \cdot v_e)^2$ owing to the normal stress proportionality. By summing all time intervals we should then obtain a total transient duration which also scales as $1/(\sigma_n \cdot v_e)^2$. Since slip rate v_e is constant, the slip distance corresponding to the transient duration (i.e., thermal slip distance d_{th}) should be obtained through multiplication by v_e , resulting in the theoretical scaling “ $d_{th} \propto 1/(\sigma_n^2 \cdot v_e)$ ”. As a consequence, by combining theoretical arguments relating the duration of transient in the pre-melt phase and duration of weakening in the post-melt phase, on the one hand, and the observation that shear stress approximately scales with normal stress in the initial sliding phases, we argue that the relation “ $d_{th} \propto 1/(\sigma_n^2 \cdot v_e)$ ” should apply. In order to test such a dependence, measures of d_{th} for various experiments under variable normal stress and variable slip rate can be done, and plotted against the corresponding value of $1/(\sigma_n^2 \cdot v_e)$. We did so in Fig. 3c and find that – within the interval of values

explored in the present experiments, and within the scatter and uncertainty of the results – the predicted dependence is verified.

4.2.4. Final re-strengthening of the slipping zone

The experiment is interrupted by removing the motor clutch and letting the machine rotate under its own inertia, until frictional dissipation achieves a complete stop a few seconds later. In this final stage we observe that the decrease in slip rate is accompanied by a marked increase in shear stress, until a peak is reached at time of complete stopping (Fig. 2a). Strength increase in the decelerating phase is compatible with the negative velocity dependence generally observed in the presence of frictional melts and predicted by theoretical models [Nielsen et al., 2008]. The reduction in heat production rate at lower velocities causes a lower melting rates (hence a thinner melt layer) and lower temperatures inside the melt (hence higher viscosity) resulting in a fault strengthening. Moreover, melt cooling triggers crystallite nucleation and overgrowth (section 4.1). The increase in content of solid particles, together with the increase in the viscosity of the melt due to cooling, might explain the abrupt increase in shear stress observed at the end of the experiment (point g in Fig. 2a). The progressive deceleration is due to the combined effect of dissipation from shear stress on the sample and mechanical friction in the rotary apparatus (essentially ball-bearing friction in the rotating parts).

The magnitude of strength recovery during the stopping stage is reduced for experiments that cumulate a larger slip [from 8 MPa for 2.77 m of slip (HVR672) to 2.9 MPa for 30.50 m of slip (HVR620), Fig. 2b]. The differences in peak of strength recovery alone are not directly related to the rock–constitutive properties; they essentially depend on the difference in shear stress at the time when deceleration starts. The amount of dissipative work required to achieve full stopping of rotary motion should be the same for all experiments performed at identical speed, regardless of the value of shear stress at the onset of deceleration and of its subsequent evolution. Different experiments were interrupted at different stages of sample evolution during its weakening. Friction under these conditions is not at the steady-state and it is not a function of velocity alone. In particular, the levels of shear stress at time of interruption differ (though velocity may be the same). Since the interruption is imposed at a different stages and under different stress levels, the subsequent evolution of the stress curves differs from one experiment to the other.

An experiment interrupted at an early stage -when the stress is still relatively high- will stop faster than another experiment interrupted later -when the stress has had time to reach a lower level during the weakening stage. Indeed a higher friction opposes sample rotation more effectively. This remains true even if both the experiments were interrupted under an identical slip velocity. As a consequence, the shear stress curve may follow higher or lower paths and reach different peak values, depending on where it stands at the onset of deceleration, but the cumulated dissipation in the decelerating phase will remain the same. Indeed, a careful analysis of the shear stress curves in the

decelerating interval reveals that the combined dissipative work is roughly constant for a given rotation speed – or moment of inertia of the rotating system – at the onset of deceleration. The dissipation combines effect of the friction on the sample (area under the shear stress curve) and that estimated from the friction in the mechanical parts of the rotary machine (about 10 % of the overall dissipation in the decelerating stage, as shown in Appendix A).

In addition, the evolution of shear stress against slip rate in this phase provides some information on the velocity dependence of friction. However, since velocity is not the only variable affecting friction in the transient state (friction depends on velocity alone only if the system is at the steady-state), such information is not unambiguous. Figure 9 represents the observed shear stress as a function of instantaneous slip velocity during the transient decelerating stage, and it is compared to a theoretical curve described by eq. 5. The theoretical dependence assumes steady-state and no loss of radiation, so the comparison is only indicative. While the steady-state curve should be considered at best as an approximation, the observed negative trend is in qualitative agreement with the expected theoretical prediction. Figure 9 can also be compared to results obtained in Figure 4b for rate-dependence under steady-state conditions.

4.3 Extrapolation of experimental data to natural conditions

The experiments described in this study were conducted at room temperature (~20 °C), low normal stresses (< 16.1 MPa) and high concentration of Oxygen (20 % in vol.). *In situ* peridotite in the mantle or lower crust is under much higher temperatures (> 600 °C, e.g., Ueda et al., 2008) and normal stresses (> 1 GPa), but lower fugacities ($fO_2 = -11$) Under these high temperatures and pressures, peridotite deformation undergoes mainly by plastic flow (e.g., dislocation and diffusion creep) at few centimeter per year [e.g., Karato, 2008]. However, during plastic flow, frictional melts might be produced once shear stress instabilities occur. Instabilities can be triggered by different processes such as (1) seismic rupture propagation in the lower crust during large earthquakes [Sibson, 1977], (2) self-localizing thermal runaway in deep-seated rocks [Braeck and Podladchikov, 2007; John et al., 2009] or (3) highly localized viscous creep in pre-existing fine-grained shear zones [Keleman and Hirth, 2007; John et al., 2009]. Field evidences support the cyclic activity of ductile shear localization (producing host mylonite), followed by a seismic slip (producing friction melts solidified in pseudotachylyte), and further ductile shear (producing ultramylonite) [Ueda et al., 2008]. Once seismic melts are produced, fault rheology is governed by the viscous-frictional properties of the melt [John et al., 2009]. Noteworthy, melt lubrication is almost independent of normal stress [e.g., Nielsen et al., 2008]. It follows that the experiments described in this study, though conducted at ambient conditions that do not reproduce the temperatures and pressures expected at mantle depth, they simulate the rheology of friction melt-bearing deep-seated faults.

However, the oxidation of olivine debris and sliding surfaces due to the high temperatures achieved at the asperity contacts during sliding, might impede the extrapolation of our experimental data to crustal and mantle conditions ($f_{O_2} = -11$), where O_2 fugacities are orders of magnitudes lower than in the laboratory ($f_{O_2} = -0.68$) [Philpotts, 1990]. Olivine can be oxidized at $T > 600$ °C into forsterite, silica, and Fe-oxides (magnetite or hematite, depending on the heating conditions), when exposed to room air [Gualtieri et al., 2003 and references therein]. Studies on the effect of oxidation products of metals (martensitic reactions in the case of iron, [Bowden and Tabor, 1950; Cocks, 1957; Lim et al., 1989]) and oxidation of iron following decomposition of siderite [Han et al., 2007b], showed that these thermally produced oxides may reduce the friction significantly at seismic slip rates. But as described in section 3.1.1., oxidation of olivine does not affect significantly the evolution of shear stress with slip (Fig. 2c). Moreover, in the experiments described here, the possible oxidation of the sliding surfaces is rapidly followed by melting, so it is the rheology of the melt that governs the bulk strength of the simulated faults for most of the duration of the experiment. We conclude that the effects of oxidizing conditions on shear strength of the simulated faults are probably negligible and the experimental data can be extrapolated to natural conditions in terms of oxygen fugacity.

We performed HVRF experiments on the Balmuccia peridotite which hosts (natural) ultramafic pseudotachylytes [Obata and Karato, 1995; Ueda et al., 2008]. Microstructures of experimentally produced pseudotachylyte such as thin melt layers, injection veins, and the formation of microlites of olivine and dendritic clinopyroxene are quite similar to the natural ones (compare Fig. 5b and 5g with Figure 4 in Obata and Karato [1995]). Actually, this is the very first time where natural and experimental microstructures are almost identical, at least in the case for frictional melting. Thus, the experiments described here well reproduce the melting processes of peridotite-bearing faults at seismic slip rates.

Shear stress evolves with slip in a complex manner during the experiments and includes two strengthening and two weakening stages (Fig. 2a). While first strengthening is probably an artifact of the experimental configuration related to the absence of an applied shear stress before sliding initiates (section 4.2.1), we might speculate that second strengthening could arrest rupture propagation in nature. However, the peak in shear stress at the end of second strengthening corresponds to a coefficient of friction of about 0.2, maybe too low to arrest rupture propagation. Moreover, the critical distance to achieve the second peak in shear stress roughly decreases with increasing normal stress (is reduced to 0.5 m at 16.1 MPa normal stress, Table 2), suggesting that it should almost disappear at the normal stresses expected at mantle depths (> 1 GPa). Also the thermal slip distance to achieve the steady-state shear stress decreases with increasing normal stress and power density, from several tens of meters at low normal stresses to few meters at larger normal stresses (Table 2 and Fig. 3). It follows that very low dynamic shear stresses should be easily achieved at mantle depths after few tens of centimeters or less in nature, so for displacements compatible with real earthquakes.

The steady-state shear stress is far below the Byerlee's law and slightly depends on normal stress (Fig. 4a), which supports melt lubrication of peridotite faults at least at the high slip rates (0.2-1.1 m/s). The extrapolation of the experimental results to natural conditions by means of Eq. 4 suggests shear stresses as low as 10 MPa at 50 km depth and, as a consequence, given the large normal stresses (> 1 GPa) expected, almost total dynamic stress drops (i.e., faults are statically strong but dynamically weak) and large slips can be achieved once seismic slip is triggered at mantle depths. The large stress drops predicted by the experimental investigations and theoretical analysis described here and resulting from melt lubrication are consistent with the field estimates from pseudotachylyte-bearing faults hosted in peridotites [Andersen et al., 2008; John et al., 2009].

5. Conclusions

To investigate the frictional melting processes and dynamic strength of peridotite faults at seismic slip rates, we performed high velocity rock friction experiments on a natural peridotite stem from Balmuccia (Italy) at slip rates of 0.23 to 1.14 m/s and normal stresses of 5 to 16 MPa. We also have performed geochemical and microstructural investigations of the experimental faults. In the experiments, we found two stages of fault strengthening, both occurring at the initiation of sliding, similarly to other experiments performed on gabbros [Tsutsumi and Shimamoto, 1997]. First strengthening cannot be investigated with the present experimental configuration. Second strengthening is associated with the production of a grain-supported melt-poor layer in the slipping zone. The two strengthening stages are alternated with two stages of slip weakening (Fig. 2a). First weakening is associated with the formation of gouge which is probably weakened by flash heating at asperity contacts of the gouge particles. Second weakening is associated with the formation of a thin and continuous melt layer decorating the slip surfaces. Second weakening evolves towards a steady-state shear stress, when the fault is fully lubricated. Since both weakening mechanisms (i.e., flash weakening and melt lubrication) are thermally activated, we introduced the thermal slip distance as the distance to achieve the steady-state shear stress. By conducting several experiments under different normal stresses and slip rates, the thermal slip distance decreased with increasing normal stress and power density. Since larger confining stresses and power densities are expected at mantle conditions, we conclude that low dynamic shear stresses should be easily (i.e., short thermal slip distances) achieved in nature.

An important outcome of the experiments described in this study and consistent with the result of other experiments performed in cohesive silicate-bearing crystalline rocks such as tonalites [Di Toro et al., 2006a] or gabbros [Hirose and Shimamoto, 2005] is that (1) shear stress at steady-state is well below than that expected by the Byerlee's law and, (2) shear stress at steady-state has very slight dependence on normal stress. The two experimental observations and the presence of frictional melts in the slipping zone imply that melt lubrication occurs on peridotite-bearing faults at seismic slip rates.

A theoretical equation based on the physical processes occurring during melt lubrication [Nielsen et al., 2008] predicts the magnitude of shear stress at steady-state.

Experiments were performed under ambient conditions that do not reproduce mantle conditions, where crystal plasticity is the dominant deformation mechanism. However, the occurrence of deep-seated earthquakes [Kanamori et al., 1998] and the evidence for cyclic production of pseudotachylytes and high temperatures ultramylonites in faults hosted in peridotites [e.g., Corsica, Western Alps: Andersen et al., 2008; Ueda et al., 2008], suggest that shear instabilities at mantle conditions occur. Shear instabilities might result in the production of frictional melts which govern the fault rheology at seismic slip rates [e.g., Keleman and Hirth, 2008; Ueda et al., 2008; John et al., 2009]. The experiments described here reproduce these deformation conditions governed by the presence of friction-induced melts. Moreover, several lines of evidence allow to extrapolate the experimental data described here to deep-seated natural conditions. These include the similarity of the microstructures (i.e., densely packed microlites of olivine and pyroxene) in natural and experimental pseudotachylyte-bearing faults and the results of experiments under argon flux which reproduce low oxygen fugacity conditions.

We conclude that since the physics of melt lubrication is somehow predictable [Nielsen et al., 2008], our experimental results might be extrapolated to the study of rupture dynamics in mantle rocks. In particular, shear stresses as low as few MPa are expected in peridotite-bearing rocks in the presence of ultramafic melts at mantle depths.

Acknowledgements

We thank the editor Patrick Taylor, Chris Marone and the associate editor John Spray for careful comments and constructive reviews. Piero Del Gaudio was granted by the FIRB – MIUR project "Sviluppo Nuove Tecnologie per la Protezione e Difesa del Territorio dai Rischi Naturali". Giulio Di Toro was granted by a Progetti di Eccellenza Fondazione Cassa di Risparmio di Padova e Rovigo (CARIPARO) and by the European Research Council Starting Grant project Nr. 205175 (USEMS). We thank Raul Carampin for EPMA analysis, Leonardo Tauro for thin section preparation and Piergiorgio Scarlato and Massimo Cocco for supporting our work.

References

- Andersen, T. B., and H. Austrheim (2006), Fossil earthquakes recorded by pseudotachylytes in mantle peridotite from the Alpine subduction complex of Corsica, *Earth Planet. Sci. Lett.* 242, 58-72.
- Andersen, T. B., K. Mair, H. Austrheim, Y. Y. Podladchikov, and J. C. Vrijmoed (2008), Stress release in exhumed intermediate and deep earthquakes determined from ultramafic pseudotachylyte *Geology* 36, 995–998.
- Beeler, N. M., T. E. Tullis, M. Blanpied, and J. Weeks (1996), Frictional behavior of large displacement experimental faults, *J. Geophys. Res.*, 101(B4), 8697-8715.
- Beeler, N. M., T. E. Tullis, and D. L. Goldsby (2008), Constitutive relationships and physical basis of fault strength due to flash heating, *J. Geophys. Res.* 113, B01401, doi:10.1029/2007JB004988.
- Bouchon, M., and P. Ihlé (1999), Stress drop and frictional heating during the 1994 deep Bolivia earthquake, *Geophys. Res. Lett.*, 26(23), 3521-3524.
- Boutareaud, S., D.-G. Calugaru, R. Han, O. Fabbri, K. Mizoguchi, A. Tsutsumi, and T. Shimamoto (2008), Clay-clast aggregates: A new textural evidence for seismic fault sliding?, *Geophys. Res. Lett.* 35, L05302, doi:10.1029/2007GL032554.
- Bowden, F. P., and D. Tabor (1950), *The Friction and Lubrication of Solids*. Clarendon Press, Oxford.
- Braeck, S., and Y. Y. Podladchikov (2007), Spontaneous thermal runaway as an ultimate failure mechanism of materials. *Phys. Rev. Lett.* 98, 095504.
- Bridgman, P.W. (1936), Shearing phenomena at high pressure of possible importance for geology, *Jour. of Geol.*, 44, 653-669.
- Byerlee, J. D. (1978), Friction of rocks, *Pure Appl. Geophys.* 116, 615-626.
- Cocks, M. (1957), Role of atmospheric oxidation in high speed sliding phenomena, *J. Appl. Phys.*, 28, 835-843.
- Costa, A. (2005), Viscosity of high crystal content melts: dependence on solid fraction, *Geophys. Res. Lett.*, 32, L22308, doi:10.1029/2005GL024303.
- Dieterich, J. H., B. D. Kilgore (1994), Direct observations of frictional contacts: new insights for state – dependent properties, *Pure Appl. Geophys.*, 143, 283-302.

- Di Toro, G., and G. Pennacchioni (2004), Superheated friction-induced melts in zoned pseudotachylytes within the Adamello tonalites (Italian Southern Alps), *J. Struct. Geol.*, 26, 1783-1801.
- Di Toro, G., D. L. Goldsby, and T. E. Tullis (2004), Friction falls towards zero in quartz rock as slip velocity approaches seismic rates, *Nature*, 427, 436-439.
- Di Toro, G., T. Hirose, S. Nielsen, G. Pennacchioni, and T. Shimamoto (2006a), Natural and experimental evidence of melt lubrication of faults during earthquakes, *Science*, 311, 647-649.
- Di Toro, G., T. Hirose, S. Nielsen, and T. Shimamoto (2006b), *Relating high-velocity rock friction experiments to coseismic slip in the presence of melts*. In Abercrombie, R., McGarr, A., Di Toro, G. & Kanamori, H., (eds) Radiated Energy and the Physics of Faulting, American Geophysical Union Monograph Series, **170**, 121-134.
- Fialko, Y., and Y. Khazan (2005), Fusion by earthquake fault friction: Stick or slip?, *J. Geophys. Res.*, 110, B12407, doi:10.1029/2005JB003869.
- Frohlich, C. (2006), *Deep earthquakes*. Cambridge University Press, Cambridge, UK, 573 pp.
- Goldsby, D. L., and T. E. Tullis (2002), Low frictional strength of quartz rocks at subseismic slip rates, *Geophys. Res. Lett.*, 29, doi:10.1029/2002GL015240, 1844.
- Griggs, D., and J. Handin (1960), Observations on fracture and a hypothesis of earthquakes. *Geological Society of America Memories*, 79, 343-373.
- Gualtieri, A. F., M. Gemmi, and M. Dapiaggi (2003), Phase transformations and reaction kinetics during the temperature-induced oxidation of natural olivine, *Am. Mineral.*, 88, 1560-1574.
- Han, R., T. Shimamoto, T. Hirose, J.-H. Ree, and J. Ando (2007a), Ultralow friction of carbonate faults caused by thermal decomposition, *Science*, 316, 878-881.
- Han, R., T. Shimamoto, J. Ando, and J.-H. Ree (2007b), Seismic slip record in carbonate-bearing fault zones: An insight from high-velocity friction experiments on siderite gouge, *Geology*, 35, 1131-1134.
- Heaton, T.H. (1990), Evidence for and implications of self-healing pulses of slip in earthquake rupture, *Phys. Earth Planet. Inter.*, 64, 1-20.

- Hirose, T., and T. Shimamoto (2003), Fractal dimension of molten surfaces as a possible parameter to infer the slip-weakening distance of faults from natural pseudotachylytes, *J. Struct. Geol.*, 25, 1569-1574.
- Hirose, T., and T. Shimamoto (2005), Growth of molten zone as a mechanism of slip weakening of simulated faults in gabbro during frictional melting, *J. Geophys. Res.*, 110, B05202, doi:10.1029/2004JB003207.
- Hirose, T., and M. Bystricky (2007), Extreme dynamic weakening of faults during dehydration by coseismic shear heating, *Geophys. Res. Lett.*, 34, L14311, doi:10.1029/2007GL030049.
- Ide, S., and M. Takeo (1997), Determination of constitutive relations of fault slip based on seismic wave analysis, *J. Geophys. Res.* 102(B12), 27379-27391.
- John. T., S. Medvedev, L. H. Rüpke, T. B. Andersen, Y. Y. Podladchikov, and H. Austrheim (2009), Generation of intermediate-depth earthquakes by self-localizing thermal runaway, *Nature Geoscience* 2, 137-140.
- Kanamori, H., D. L. Anderson, and T. H. Heaton (1998), Frictional melting during the rupture of the 1994 Bolivian Earthquake, *Science*, 279, 839-842.
- Karato, S. I. (2008), *Deformation of Earth Materials*. Cambridge University Press. 463 pp.
- Kelemen, P. B., and G. Hirth (2007), A periodic shear-heating mechanism for intermediate-depth earthquakes in the mantle, *Nature*, 446, 787-790.
- Lim, S. C., M. F. Ashby, and J. H. Brunton (1989), The effect of sliding conditions on the dry friction of metals, *Acta Metal.*, 37, 767-772.
- Marone, C. and B. Kilgore (1993), Scaling of the critical slip distance for seismic faulting with shear strain in fault zones. *Nature*, 362, 618-622.
- Marone, C. (1998), Laboratory-derived friction laws and their application to seismic faulting, *Ann. Revs. Earth Plan. Sci.*, 26, 643-696.
- Mizoguchi, K., T. Hirose, T. Shimamoto, and E. Fukuyama (2007), Reconstruction of seismic faulting by high-velocity friction experiments: An example of the 1995 Kobe earthquake, *Geophys. Res. Lett.*, 34, L01308, doi:10.1029/2006GL027931.

- Nielsen, S., G. Di Toro, T. Hirose, and T. Shimamoto (2008), Frictional melt and seismic slip, *J. Geophys. Res.*, 113, doi:10.1029/2007JB005122.
- Obata, M., and S. Karato (1995), Ultramafic Pseudotachylite from the Balmuccia Peridotite, Ivrea Verbano Zone, Northern Italy, *Tectonophysics*, 242, 313-328.
- Ogawa, M. (1987), Shear instability in a viscoelastic material as the cause of deep focus earthquakes, *J. Geophys. Res.*, 92(B13), 13801-13810.
- Ohnaka, M. (2003), A constitutive scaling law and a unified comprehension for frictional slip failure, shear fracture of intact rock, and earthquake rupture, *J. Geophys. Res.*, 108, doi: 10.1029/2002JB000123.
- Paterson, M. S., and T.-F. Wong (2005), *Experimental rock deformation—The brittle field* (second edition): Berlin, Heidelberg, Springer-Verlagp. 348 pp.
- Persson, B. N. J. (2000), *Sliding Friction: Physical Principles and Applications*. Springer, Heidelberg, Germany.
- Philpotts, A. R. (1990), *Principles of Igneous and Metamorphic Petrology*. Prentice Hall, New Jersey 498 pp.
- Piccardo, B. G., G. Ranalli , M. Marasco, and M. Padovano (2008), Ultramafic pseudotachylites in the Mt. Moncuni peridotite (Lanzo Massif, western Alps): tectonic evolution and upper mantle seismicity, *Periodico di Mineralogia*, 76, 181-197 .
- Reid, H. F. (1910), The Mechanics of the Earthquake. Vol. II of *The California Earthquake of April 18, 1906*, Report of the State Earthquake Investigation.
- Rempel, A. W. (2006), *The effects of flash-weakening and damage on the evolution of fault strength and temperature, Radiated Energy and the Physics of Faulting*, Geophysical Monograph Series Vol. 170, edited by. Abercrombie, R., A. McGarr., G. Di Toro and H. Kanamori, pp. 263-270, AGU, Washington, D.C., USA.
- Rice, J. R. (2006), Heating and weakening of faults during earthquake slip, *J. Geophys. Res.*, 111, doi:10.1029/2005JB004006.
- Scholz, C. H. (2002), *The Mechanics of Earthquakes and Faulting*. 2nd ed.. Cambridge, New York, Melbourne: Cambridge University Press, 471 pp.

- Shimamoto, T., and A. Tsutsumi (1994), A new rotary-shear high-speed frictional testing machine: its basic design and scope of research, *Struct. Geol., J. Tect. Res. Group of Japan*, 39, 65–78.
- Sibson, R. H. (1977). Fault rocks and fault mechanisms. *Journal of the Geological Society of London* 133, 191-213.
- Spray, J. G. (1987), Artificial generation of pseudotachylyte using friction welding apparatus: simulation of melting on a fault plane, *J. Struct. Geol.*, 9, 49-60.
- Spray, J. G. (1992), A Physical Basis for the Frictional Melting of Some Rock- Forming Minerals, *Tectonophysics*, 204, 205-221.
- Spray, J. G. (1993), Viscosity determinations of some frictionally generated silicate melts: implications for fault zone rheology at high strain rates, *J. Geophys. Res.*, 98, 8053-8068.
- Spray, J. G. (1995), Pseudotachylyte controversy: fact or friction? *Geology*, 23, 1119-1122.
- Spray, J. G. (2005), Evidence for melt lubrication during large earthquakes, *Geophys. Res. Lett.*, 32, L07301, doi:10.1029/2004GL022293.
- Tsutsumi, A., and T. Shimamoto (1997), High-velocity frictional properties of gabbro, *Geophys. Res. Lett.*, 24 (6), 699-702.
- Tullis, T. E. (2008), Friction of Rock at Earthquake Slip Rates. In Vol. 4 of the Treatise of Geophysics, *Earthquake Seismology*, edited by H. Kanamori. Elsevier, Amsterdam.
- Ueda, T., M. Obata, G. Di Toro, K. Kanagawa, and K. Ozawa (2008), Mantle earthquakes frozen in mylonitized ultramafic pseudotachylytes of spinel-lherzolite facies, *Geology*, 36 (8), 607-610.

Appendix A: Motion arrest and dissipation after motor interruption

Motion arrest occurs when the inertia of the rotating system (machine parts in motion, sample holder, sample) with kinetic energy E_k is dissipated by frictional work W_f (on the sample sliding surface) and by overall mechanical dissipation of the machine W_m (essentially due to friction in the ball bearings of rotating parts):

$$E_k = W_f + W_m$$

Since the machine's moment of inertia is constant, the kinetic energy E_k at the beginning of deceleration (time of motor interruption t_0) only depends on the velocity $v_e(t_0)$. As a consequence the arresting work ($W_f + W_m$) should be equal for all experiments with the same $v_e(t_0)$. For a given contact surface S on the sample, and assuming a constant dissipation coefficient γ in the machine, we may write:

$$W_f = S \int_{t_0}^{t_a} \tau(t) v_e(t) dt \approx S \sum_{i=t_0/\delta t}^{t_a/\delta t} \tau(i) \cdot v_e(i) \cdot \delta t$$

$$W_m = \gamma \cdot \int_{t_0}^{t_a} v_e(t) dt \approx \gamma \cdot U_{arrest}$$

where U_{arrest} is the slip cumulated during the arresting deceleration, δt is the sampling time interval and i the time step of the experimental measure. Both W_f and U_{arrest} are directly measured in the experiments. For each experiment interrupted at a given velocity $v_e(t_0)$ we obtain an equation of two unknowns E_k and γ , which we can retrieve for a series of N experiments by minimizing the misfit of the system:

$$\left[W_f + \gamma U_{arrest} = E_k \right]_{n=1,N}$$

(where n is the experiment number). We find that the mechanical dissipation $\gamma \cdot U_{arrest}$ of the apparatus contributes as a small, but not insignificant portion (about 10 %) of the total work which induces the rotation arrest.

Table & Figure captions

Table 1. Modal mineralogy of the peridotite from Balmuccia (Italy) used in the HVRF experiments. Modal content was determined by point counting on microphotographs. Opaque mineral is mainly spinel (see Table 4).

Table 2. Experimental conditions and mechanical data for series A HVRF experiments.

Table 3. Experimental conditions and mechanical data for series B HVRF experiments.

Table 4. Electron Probe Micro-Analyzer (EPMA) composition of the main minerals of the Balmuccia peridotite (see Table 1). The first two columns compare the Energy dispersive X-ray (EDS) analyses with EPMA analyses for olivine to show the consistency of the results obtained with the two analytical techniques.

Table 5. Energy dispersive X-ray (EDS) composition of the glasses. EDS analyses are averages of representative selected analyses over the 1000 collected. Analyses are grouped according to the total displacement of the experiment and to the position of the glass inside the sample, both in the slipping zone (group 1-2) and in the wall rocks (groups 2-9). Acronyms are: s.z. = slipping zone, ol = olivine, di = diopside, spl = spinel, en = enstatite.

Fig. 1. (a) Schematic diagram of a specimen assembly for high-velocity friction experiments. The diagram shows also the position and orientation of the thin-section. **(b)** Photograph of the specimen mounted in the apparatus. Rotational side (left) rotates clockwise up to 1500 rounds per minute. Torque is measured with a torque gauge located just behind the specimen holder of the stationary side (right). Note the gap between two aluminum rings to avoid metal-metal friction that may contaminate the accurate determination of peridotite frictional strength.

Fig. 2. Mechanical data from high-velocity rock friction experiments. **(a)** Typical shear stress versus slip curve for peridotite at a constant normal stress of 13 MPa (series A experiments: HVR644, Table 2). Two stages of slip weakening are recognized (a to b and c to d). At point g, a magnetic clutch turns off so that a fault slips by inertia, resulting in strength recovery as slip rate decreases (see section 4.2.4). Grey line is a best fit smoothed curve which allows to estimate (see main text) a thermal slip distance d_{th} of 11.27 ± 1.24 m in the tract a – d. Steady-state shear stress is achieved in sections d – e and f – g: note the increase in shear stress when the imposed slip rate decreases from 0.92 to 0.61 m/s (points e – f). **(b)** Shear stress versus slip curves at a constant normal stress of 13.0 MPa and slip rate of 1.14 MPa with increasing cumulative slip (series B experiments, Table 3). Steady-state shear stress is achieved in HVR673 and HVR620. **(c)** Comparison of shear stress versus slip curves for experiments performed at room air (oxidizing conditions, HVR620 and HVR652) and under Ar flow (HVR651) at normal stress of 13.0 MPa and slip rate of 1.14 m/s. No significant effect of oxidization on fault strength was observed. In HVR652, the radiation thermometer yielded a temperature of the outer surface of the slipping zone of 1100 ~ 1300°C at steady-state. Temperature data above 1240°C were not recorded because the temperature output exceeded a voltage scale limit set by a digital recorder.

Fig. 3. Thermal slip distance d_{th} plotted against **(a)** slip rate, **(b)** normal stress and **(c)** $1/(\sigma_n^2 v_e)$ (see text for description). In Figure c, data are from experiments performed at slip rates of 1.14 m/s unless when specified.

Fig. 4. Shear stress at the initial peak, second peak and steady-state plotted against **(a)** normal stress and **(b)** slip rate. **(a)** Data from experiments performed at a constant slip rate of 1.14 m/s. A nearly linear relationship holds within experimental conditions: $\tau_i = 0.6 \cdot \sigma_n$ for initial peak and $\tau_{2nd} = 2.13 + 0.21 \cdot \sigma_n$ (correlation coefficient = 0.88) for second peak. The best fit for steady-state shear stress data with Eq. 4 is $\tau_{ss} = 1.14 \cdot (\sigma_n - 4.69)^{0.25}$ (correlation coefficient = 0.81). Byerlee's friction law, $\tau = 0.85 - 0.6 \cdot \sigma_n$, is shown in gray as reference. **(b)** Data from experiments performed at a constant normal stress of 13 MPa. The second peak in shear stress is almost independent to normal stress. The best fit for steady-state shear stress data is described as $\tau_{ss} = (v_e / 2.8)^{-0.5}$ (correlation coefficient = 0.82) (see text for description).

Fig. 5. Microstructures in experimental fault zones in peridotites (Backscattered electron, BSE, FE-SEM images) from runs stopped at different stages. **(a)** HVR675, second strengthening, 1.5 m of slip: fault gouge partially welded by ultra-thin layers and micro-patches of glass (usually 100 nm in thickness) with pumiceous and bubbly aspect. The gouge is made of angular to rounded fragments. **(b)** HVR672, about second peak in strength, 2.7 m of slip: small, zoned, euhedral grains of olivine. **(c)** HVR672, about second peak in strength, 2.7 m of slip: large view of the slipping zone showing rounded and euhedral grains immersed in glass matrix. Fragment grain size decreases towards the wall rocks. Note the darker color of the slipping zone/wall rock boundary due to Fe diffusion loss in olivine. **(d)** HVR672, about second peak in strength, 2.7 m of slip: slipping zone at the contact with diopside in the wall rocks. Zoned olivine fragments and microlites are immersed in the glass, both in the slipping zone and in the veins intruding the wall rock. **(e)** HVR673, second weakening, 9.9 m of slip: slipping zone with zoned fragments and euhedral microlites of olivine. A large spinel grain survived from melting due to its higher melting point. **(f)** HVR620, steady-state, 30.5 m of slip: slipping zone with different types of glass (brighter in the bottom left). Note the large amount of zoned microlites and fragments. **(g)** HVR644, steady-state, 48.6 m of slip: slipping zone with dendritic and skeletal crystals of clinopyroxene, crystallized from the friction melt. Olivine euhedral grains are zoned. **(h)** HVR620, steady-state, 30.5 m of slip: large view which includes the slipping zone and the fracture network filled by glass veins in the wall rocks (bright in color). Veins are due to melt injection from the slipping zone and from melt produced *in situ* (mainly diopside preferential melting in the wall rocks). Glass veins spread till about 500 μm from the slipping zone, and they were observed up to 900 μm in the same sample. Acronyms are: ol = olivine; di = diopside; Cr-spl = Chromium spinel; gl = glass; HR = host rock.

Fig. 6. Olivine grains from the slipping zone (BSE images) and EDS FeO and CaO transects. In the interpretation of these EDS data we considered only the analyses collected at more than 500 nm from the grain border, as the EDS beam spot size was of 400 nm. **(a)** Olivine grains with a Fe-rich core and Fe-poor rim (LG4 and LG5) from HVR675 (1.53 m of slip). **(b)** Olivine grains with Fe-rich core (LG11 and LG12; note the zoning of LG11 in the nearby FE-SEM image) from HVR620 (30.50 m of slip). **(c)** Olivine grains with Fe-poor core (LG13 and LG14) from HVR620 (30.50 m of slip).

Fig. 7. Slipping zone in peridotite under the optical microscope (HVR620).

Fig. 8. Evolution of the composition of major elements of the glass with increasing slip. Data are from series B experiments performed at constant slip rate of 1.14 m/s and normal stress of 13 MPa. **(a)** SiO₂% evolution with slip. **(b)** CaO, FeO and Al₂O₃ percentages evolution with slip. See text for discussion.

Fig. 9. Evolution of shear stress with slip rate for two samples from series B at final stage (deceleration after motor clutch is disconnected).

Table 1

Mineralogy	%
Olivine	70.9
Clinopyroxene	20.9
Orthopyroxene	4.4
Opaque	3.9
total	100.0

Table 2

Run No	Normal stress	Total disp.	Slip rate step				Steady-state shear stress**				Coefficient of friction		Shear stress		Slip to achieve the second peak***	Thermal slip distance, d_{th}^{***}
			1st	2nd	3rd	4th	1st	2nd	3rd	4th	initial peak	second peak	initial peak	second peak		
			m/s	m/s	m/s	m/s	MPa	MPa	MPa	MPa			MPa	MPa		
HVR623	15.6	35.00	1.14	-	-	-	2.39	-	-	-	0.403	0.340	6.23	5.51	0.63	10.80 ± 2.12
HVR633	16.1	29.95	1.14	-	-	-	2.66	-	-	-	0.602	0.330	8.93	5.51	0.51	4.80 ± 0.79
HVR634	7.8	49.95	1.14	-	-	-	1.34	-	-	-	0.630	0.508	4.96	3.57	1.35	20.37 ± 8.04
HVR635	5.4	71.01	1.14	-	-	-	1.02	-	-	-	0.520	0.367	2.63	3.33	2.12	37.72 ± 16.28
HVR640	10.4	49.77	1.14	-	-	-	1.45	-	-	-	0.573	0.263	5.96	4.11	2.12	13.54 ± 5.15
HVR676*	13.0	40.01	1.14	-	-	-	1.85	-	-	-	0.450	0.288	5.85	5.33	0.60	10.96 ± 3.71
HVR677*	13.0	24.19	0.76	-	-	-	1.78	-	-	-	0.430	0.358	5.59	4.87	1.09	17.21 ± 2.21
HVR621	10.4	55.01	1.14	0.71	0.55	0.4	1.73	2.03	2.02	2.30	0.514	0.436	5.30	4.95	0.92	15.12 ± 2.52
HVR641	13.0	60.11	1.14	0.67	0.43	-	1.94	2.17	2.59	-	0.691	-	8.86	-	-	9.36 ± 6.48
HVR642	13.0	58.04	0.39	0.64	0.9	-	2.55	1.40	-	-	0.550	0.357	7.16	4.95	1.30	-
HVR643	13.0	44.40	0.23	0.55	-	-	3.24	2.03	-	-	0.678	-	8.82	-	-	22.79 ± 6.34
HVR644	13.0	56.12	0.92	0.61	-	-	1.76	2.01	-	-	0.690	0.333	8.98	4.71	1.79	11.27 ± 1.24
HVR645	13.0	64.29	0.76	0.47	-	-	2.16	2.55	-	-	0.648	-	8.43	-	-	16.09 ± 1.69
HVR652*	13.0	52.01	1.14	0.37	-	-	1.64	-	-	-	0.613	0.360	7.98	4.83	0.82	11.37 ± 0.96
HVR620****	13.0	30.50	1.14	-	-	-	1.67	-	-	-	0.504	0.347	6.49	4.75	0.75	11.52 ± 2.11
HVR651****	13.0	31.31	1.14	-	-	-	1.98	-	-	-	0.686	0.373	8.92	4.77	1.27	9.68 ± 0.59

* temperature measurement during run.

** Steady-state shear stress was averaged over 13 m of slip. The s.d. for all data is less than 0.1 MPa

*** the slip could not be determined in some experiments due to fluctuation of strength by breakage of specimen edge at the initiation of sliding

**** HVR620 and HVR651 appear also in Table 3

Table 3

Run No	Normal stress	Slip rate	Total slip	Coefficient of friction		Shear stress			Thermal slip distance, d_{th}	Ave. thickness of molten layer	Effective viscosity	Ave. shear strain	Estimated clasts + microlites fraction	Remarks
				initial peak	second peak	initial peak	2nd peak	steady state						
	MPa	m/s	m			MPa	MPa	MPa	m	μm	Pa s	$10^3/s$	%	
HVR675	13.0	1.14	1.53	0.660	-	8.59	-	-	-	65.9*			56-77	sample edge broke
HVR672	13.0	1.14	2.77	0.690	0.441	8.98	5.73	-	-	126.5**			56-78	around second peak
HVR671	13.0	1.14	5.70	0.690	0.422	8.98	5.48	-	-	38.4	87.92	29.69	74	weakening stage
HVR673	13.0	1.14	9.90	0.690	0.448	8.98	5.83	2.36	5.20 ± 0.75	49.8	103.09	22.89	72-76	nearly steady state
HVR620	13.0	1.14	30.50	0.503	0.347	6.54	4.75	1.67	11.52 ± 2.11	131.1	192.05	8.70	54-64	steady state
HVR651	13.0	1.14	31.31	0.686	0.373	8.92	4.77	1.98	9.68 ± 0.59	112.0	194.53	10.18	68-72	steady state, Ar flowing

* the slipping zone consists of gouge partially welded by ultra-thin glass layers and patches.

** The slipping zone is a glass supported matrix with gouge preserved in pockets.

Table 4

	Olivine EPMA		Olivine EDS		Orthopyroxene EPMA		Clinopyroxene EPMA		Cr-Spinel EPMA	
	n = 14	s.d.	n = 43	s.d.	n = 4	s.d.	n = 4	s.d.	n = 4	s.d.
Na ₂ O	0.01	0.00	0.00	0.00	0.07	0.05	1.16	0.22	0.03	0.02
MgO	48.94	0.30	47.73	1.14	33.06	0.47	15.75	0.90	18.19	0.65
Al ₂ O ₃	0.01	0.01	0.07	0.20	3.12	1.26	4.96	1.51	56.38	1.28
SiO ₂	41.54	0.34	41.08	1.12	56.46	0.94	53.13	1.14	0.05	0.03
K ₂ O	0.01	0.00	0.07	0.09	0.00	0.01	0.01	0.01	0.01	0.01
CaO	0.02	0.01	0.14	0.26	0.96	0.62	22.71	0.31	0.01	0.01
Cr ₂ O ₃	0.03	0.02	0.18	0.24	0.34	0.13	0.66	0.22	11.83	0.70
FeO	9.23	0.29	9.64	1.68	6.30	0.33	2.38	0.07	13.60	1.35
MnO	0.16	0.03	0.22	0.29	0.14	0.03	0.08	0.05	0.10	0.02
TiO ₂	0.02	0.02	0.17	0.24	0.07	0.04	0.33	0.08	0.04	0.01
P ₂ O ₅	-	-	0.13	0.16	-	-	-	-	-	-
NiO	0.36	0.04	0.56	0.71	0.05	0.01	-	-	-	-
Total	100.24	0.35	100.00	0.00	100.54	1.11	101.17	0.21	100.24	0.51

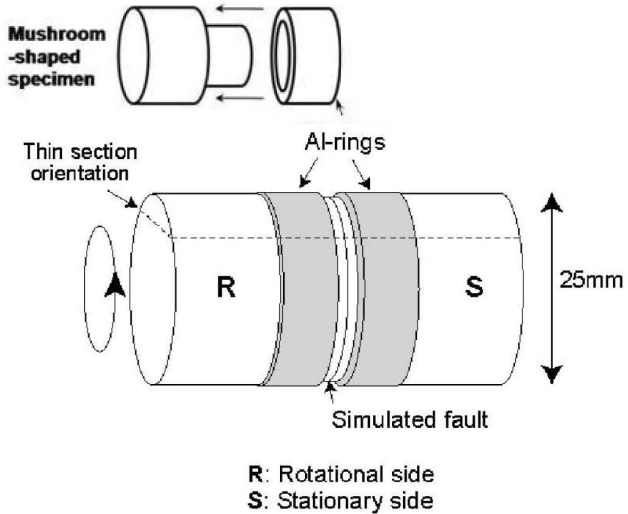
n: number of analysis; s.d.: standard deviation.

Table 5

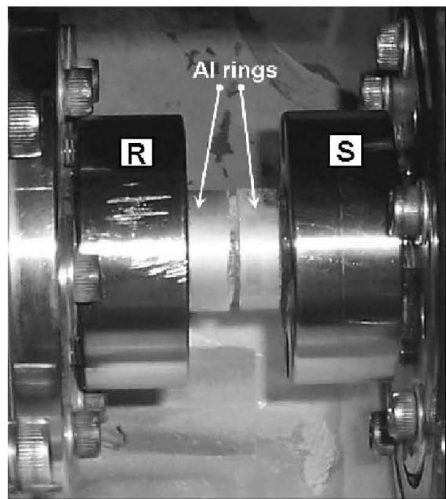
Displac.	Group 1				Group 2				Group 3											
	Glass in slipping zone				Glass near ol - ultrabasic				Glass vein in ol											
	in slipping zone		in the wall rocks		in slipping zone		in the wall rocks		in slipping zone		in the wall rocks									
	HVR675	HVR672	HVR673	HVR620	HVR675	HVR673	HVR620	HVR675	HVR672	HVR673	HVR620									
n=1	n=3	n=2	n=13	n=2	n=2	n=4	n=1	n=2	n=3	n=8										
1.57	2.77	9.90	30.50	1.57	9.90	30.50	1.57	2.77	9.90	30.50										
	std.dev.	std.dev.	std.dev.	std.dev.	std.dev.	std.dev.	std.dev.	std.dev.	std.dev.	std.dev.	std.dev.									
Na ₂ O	0.54	0.46	0.07	0.36	0.06	0.60	0.43	0.00	0.00	0.00	0.00	0.00	0.00	0.44	0.33	0.13	0.17	0.16	0.40	0.29
MgO	16.57	23.11	1.21	13.27	1.10	14.58	4.31	35.47	0.20	40.26	1.94	40.57	2.06	11.58	18.06	3.24	19.41	1.04	9.38	2.13
Al ₂ O ₃	7.64	7.30	1.35	8.66	0.48	8.84	1.14	2.98	0.21	0.05	0.06	0.28	0.56	8.65	6.98	0.59	8.55	3.10	9.32	2.21
SiO ₂	49.51	53.50	3.06	56.09	0.01	56.88	2.48	48.88	1.04	40.00	0.69	39.14	1.92	59.46	52.34	1.00	51.00	3.61	59.45	1.90
K ₂ O	0.12	0.40	0.08	0.00	0.00	0.06	0.08	0.00	0.00	0.00	0.00	0.20	0.03	0.00	0.06	0.07	0.04	0.05	0.05	0.08
CaO	6.28	7.93	2.29	11.91	0.26	11.74	1.42	3.20	0.08	0.15	0.05	0.21	0.33	7.97	10.61	0.74	10.35	2.46	9.13	1.25
Cr ₂ O ₃	6.14	0.37	0.37	0.06	0.05	0.51	0.36	0.27	0.31	0.08	0.09	0.06	0.11	0.22	0.36	0.46	0.44	0.22	0.48	0.46
FeO	11.78	5.97	5.97	9.00	0.11	6.18	0.94	8.85	0.46	18.55	2.26	17.51	2.55	11.48	10.09	0.84	9.26	3.01	10.61	0.89
MnO	0.60	0.17	0.24	0.16	0.01	0.46	0.28	0.00	0.00	0.58	0.04	0.49	0.43	0.00	0.54	0.20	0.20	0.18	0.17	0.23
TiO ₂	0.81	0.47	0.26	0.17	0.12	0.50	0.32	0.37	0.19	0.00	0.00	0.33	0.30	0.20	0.35	0.28	0.46	0.40	0.39	0.27
Tot	100.00	100.00		100.00		100.00		100.00		100.00		100.00		100.00	100.00		100.00		100.00	

Table 5

	Group 4		Group 5		Group 6		Group 7		Group 8		Group 9				
	Glass vein in ol & di		Glass vein in ol & spl		Glass vein in en		Glass vein in ol & en		Glass vein in di		Glass vein at di contact				
	HVR620		HVR620		HVR673		HVR620		HVR673		HVR620				
	n=10		n=16		n=2		n=13		n=2		n=2				
Displac.	30.50		30.50		9.90		30.50		9.90		30.50				
	std.dev.		std.dev.		std.dev.		std.dev.		std.dev.		std.dev.				
Na ₂ O	4.31	0.47	0.59	0.21	0.50	0.04	0.74	0.16	1.08	0.63	0.40	1.85	0.46	1.56	0.16
MgO	6.45	1.91	7.71	1.65	14.12	0.93	9.92	3.35	5.90	26.64	1.39	8.35	0.07	9.30	1.50
Al ₂ O ₃	19.18	1.68	15.50	1.99	9.22	0.16	8.04	0.82	11.39	5.30	0.23	19.16	1.37	6.28	0.40
SiO ₂	52.25	2.03	54.86	2.28	55.19	0.05	62.47	1.73	60.21	48.28	0.30	48.88	0.68	55.27	0.46
K ₂ O	0.17	0.17	0.09	0.12	0.00	0.00	0.03	0.05	0.36	0.02	0.03	0.10	0.13	0.04	0.06
CaO	9.98	0.72	8.49	0.69	11.51	0.28	11.89	0.92	10.42	12.05	0.04	11.18	0.13	22.29	0.86
Cr ₂ O ₃	0.60	0.97	0.62	0.59	0.10	0.13	0.51	0.30	0.00	0.40	0.13	0.69	0.53	n.d.	n.d.
FeO	4.80	0.51	10.90	0.78	8.87	1.41	5.93	0.92	9.99	5.71	0.61	7.81	0.07	4.47	0.55
MnO	0.18	0.22	0.37	0.33	0.22	0.08	0.20	0.28	0.02	0.27	0.06	0.33	0.34	0.43	0.28
TiO ₂	1.67	0.33	0.32	0.27	0.17	0.01	0.27	0.20	0.63	0.43	0.22	1.58	0.30	0.38	0.02
Tot	100.00		100.00		100.00		100.00		100.00	100.00		100.00		100.00	

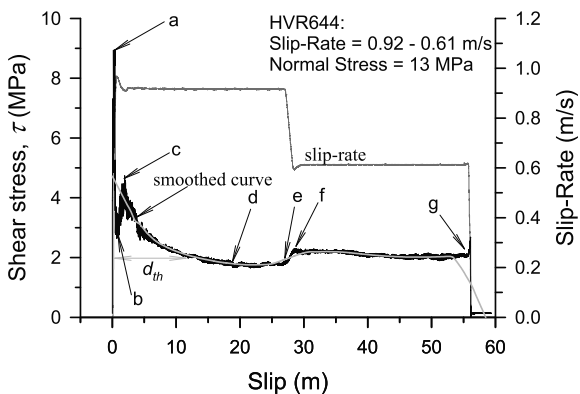


(a)

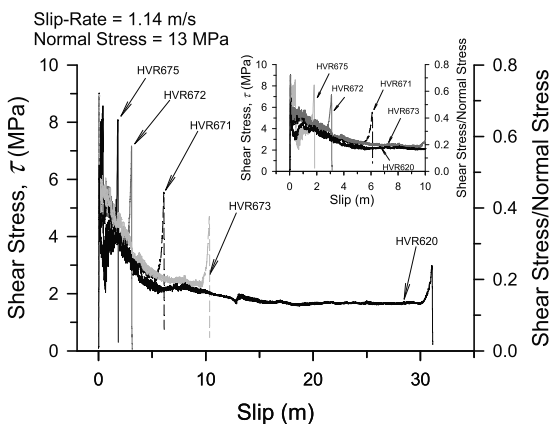


(b)

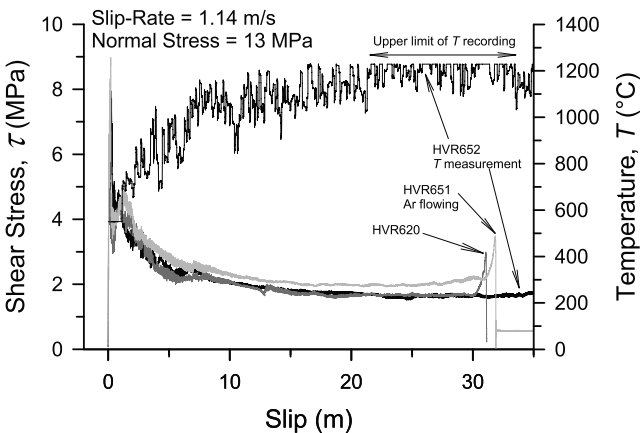
a)

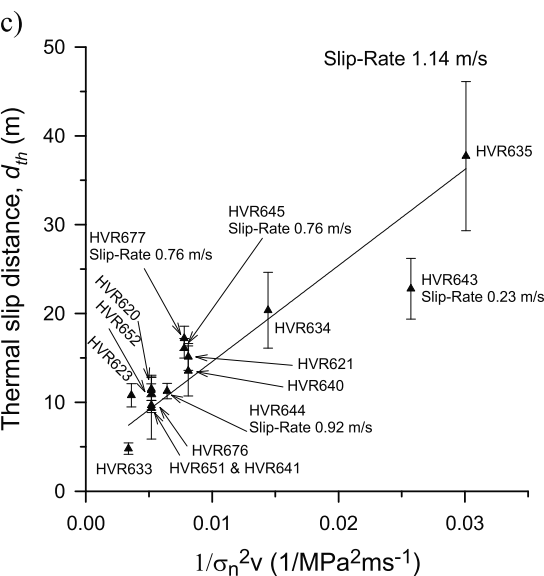
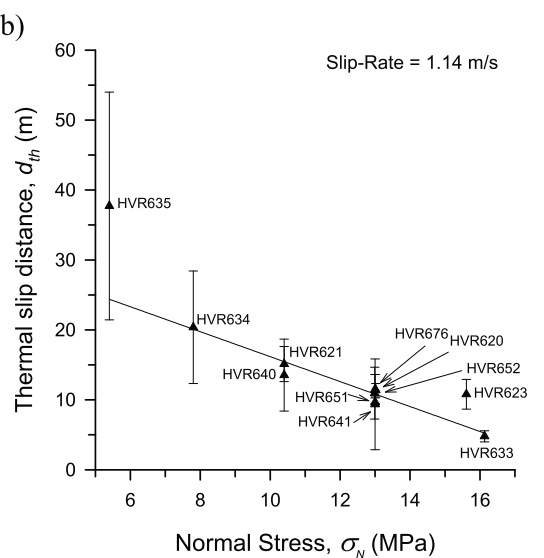
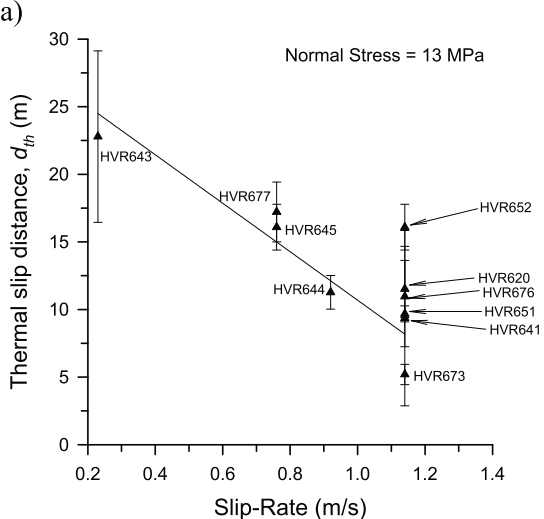


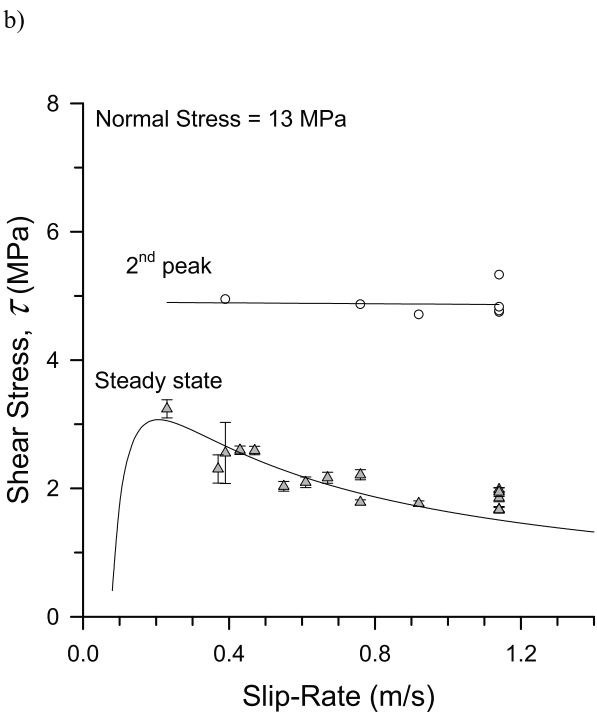
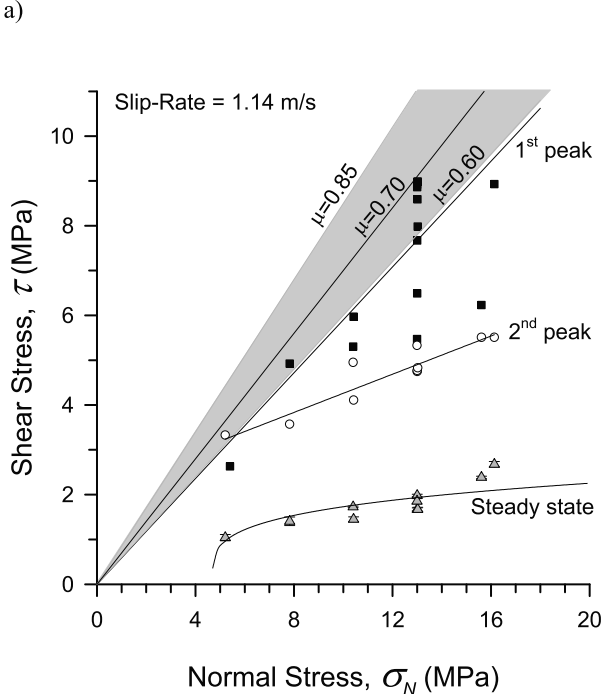
b)

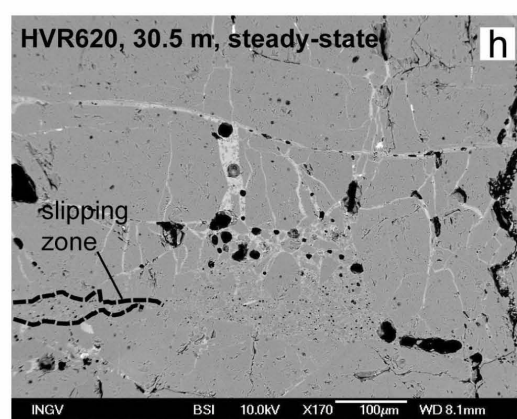
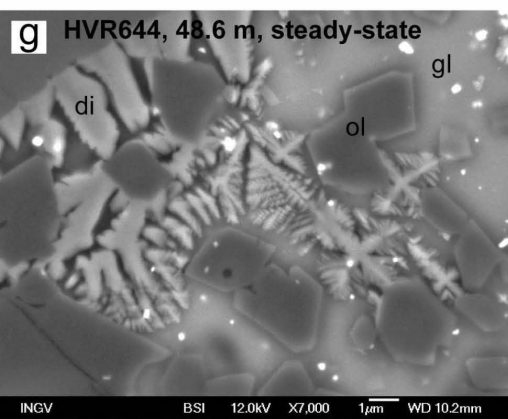
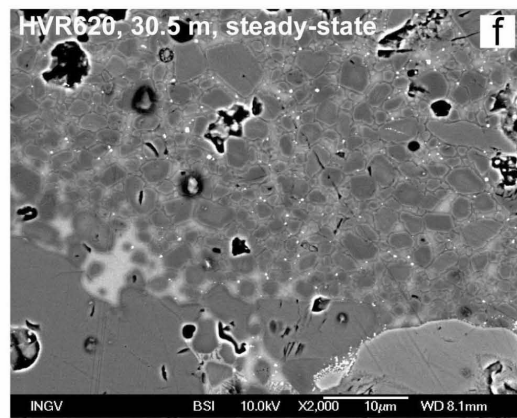
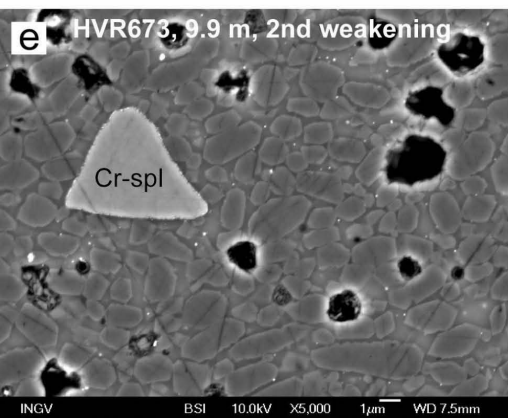
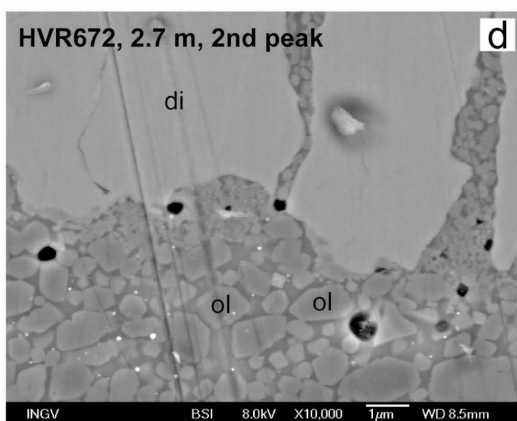
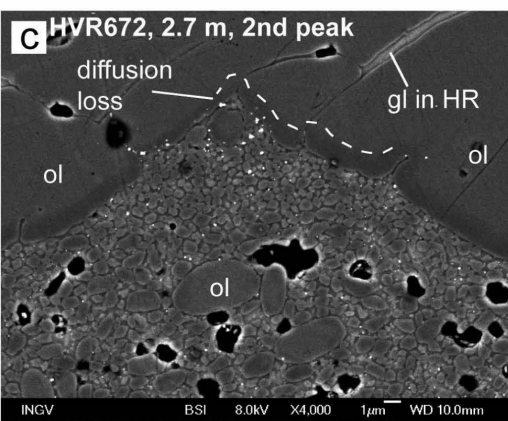
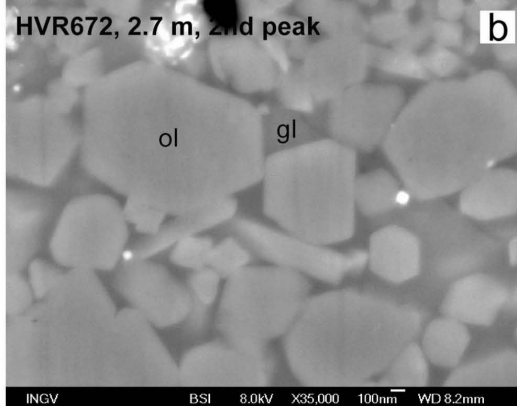
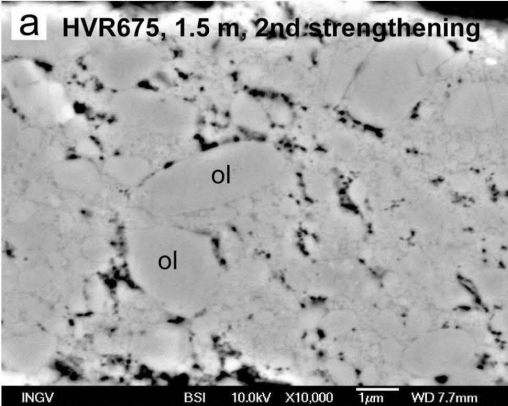


c)

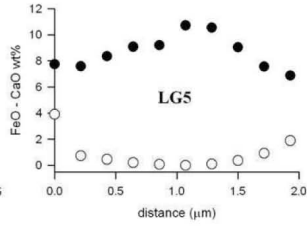
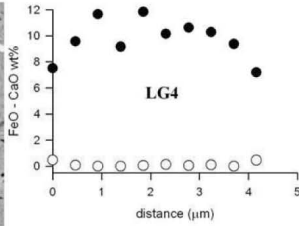
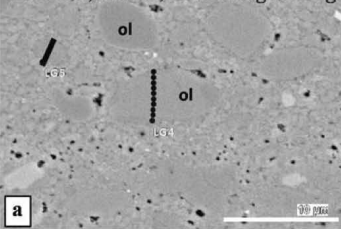






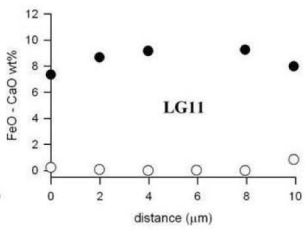
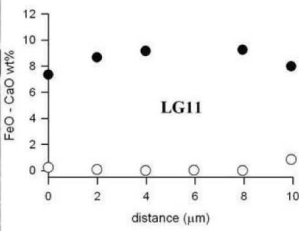
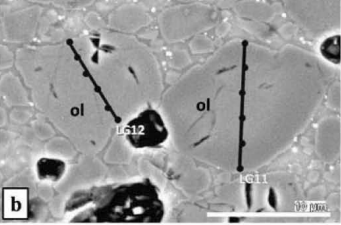


HVR675, 1.53 m, 2nd strengthening

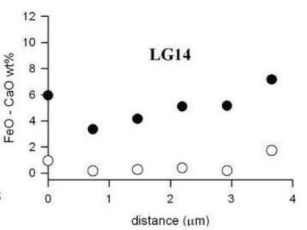
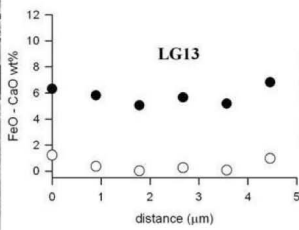
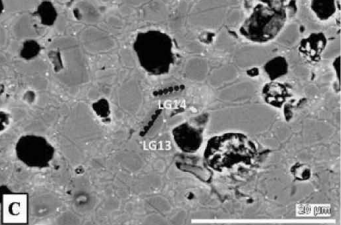


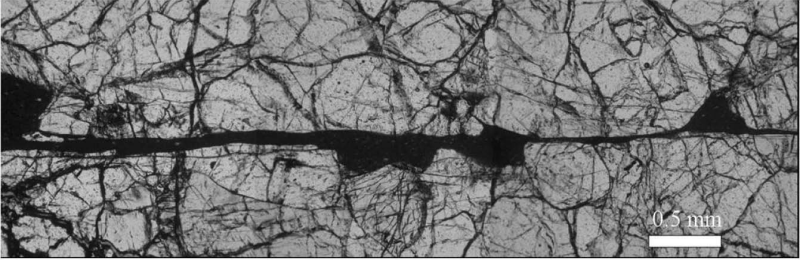
● FeO
○ CaO

HVR620, 30.50 m, steady-state



HVR620, 30.50 m, steady-state





0.5 mm

